Steady bilayer channel and free-surface isothermal film flow over topography

A.A. ABDALLA[a], S. VEREMIEIEV[b,*], P.H. GASKELL[b]

[a] *Department of Mechanical Engineering, University of Benghazi, Benghazi, Libya*
[b] *Department of Engineering, Durham University, Durham, DH1 3LE, UK*

Abstract

Two flow configurations, involving bilayers, are explored systematically: through an inclined channel comprised of two planar surfaces in parallel alignment and down an inclined plane. Both liquid layers are assumed to be perfectly immiscible and the lower rigid bounding surface contains locally defined steep-sided topographical features – either a step-up/-down or a trench/peak. A common governing equation-set based on the long-wave approximation and depth-averaging is derived, embodying the more general case of a system of n-layers, and solved numerically.

Results for the particular case of flow in a vertically aligned channel are found to be indistinguishable from corresponding solutions in the literature; those for the case of a step-up and non-zero Reynolds number having not been reported hitherto. New to this, the case of flow in a inclined channel is investigated as is the situation when, in horizontal alignment, the channel's upper planar bounding surface moves with a constant speed inducing a shear flow.

Gravity-driven bilayer film flow reveals a number of interesting features dependent on the fluid properties, the Reynolds number and the ratio of the upper to lower liquid layer thickness, with parallels drawn to the practically relevant cascade/slide-coating mode of multi-layer thin-film deposition. In the limit when both layers have identical properties the corresponding equivalent single layer solution is recovered exactly.

Keywords: Bilayers, Interfacial and free-surface flow, Topography, Fluid mechanics, Mathematical modelling, Numerical solution

1. Introduction

Film flow involving one or more contiguously adjacent liquid layers, in the presence of surface topography, features in numerous processes of industrial relevance. These include, for example, the manufacture of micro-scale sensors and devices, [1], thin-film transistors, [2], OLED displays, [3], printed circuits, [4], and the formation of functional coatings comprised of different layers deposited simultaneously, using slot-die and slide/cascade arrangements, [5]. It has motivated numerous investigations, experimental and theoretical, over the past 30 years or so as to the affect of surface topography on thin film flow, directed primarily at understanding

*Corresponding author: s.veremieiev@durham.ac.uk

the gravity-driven flow of single layer films open to the atmosphere and about which much of the basic physics involved is now well understood. The topography explored include local, trench/peak and step-up/-down features, and the same repeated periodically; experimental data has remained scarce, [6–9], while modelling and prediction have relied heavily on lubrication theory, [10–14], with the odd attempt made to address the problem more generally by solving the Navier-Stokes equations, [15–17], or Stokes flow, [18–21].

Confined channel flow involving topographical features has received far less attention, yet it clearly has a lot in common with its free-surface counterpart, particularly for bilayer flow when the properties of the upper-most layer are negligible relative to the lower layer and thick enough by comparison; in which case the influence of a planar upper channel surface on the flow due to the presence of topography on the lower surface is negligible. A rare example of just such a problem is found in the work of [22] and [23], concerning bilayer flow at the limits when both layers have the same properties and when the upper one is effectively absent compared to the lower one.

Lenz and Kumar [22] investigated steady bilayer flow in a channel containing step topography on one of the confining surfaces, using lubrication theory to derive a single third-order partial differential equation in order to describe the behaviour of the liquid-liquid interface. Solving the equation numerically they found the density ratio and thickness ratio to influence strongly the interface profile, with viscosity having a less significant effect. Comparison with equivalent single-layer gravity-driven film flow revealed that capillary features are suppressed at the interface under certain flow conditions. More recently, [23] extended the above work to include inertial effects; using a diffuse-interface method. However, the work was only partially successful in that they were able to explore flow over step-down but not step-up topographical features. Their reason for this was attributed to either a lack of sufficient numerical resolution or the choice of initial conditions. For multilayer flow the study of interest is the one by [24] that considers the instability of thin liquid trilayers in a confined channel. Other related work includes that of [25], who studied steady bilayer flow in a narrow channel of variable width revealing that for a converging channel and low viscosity ratio the pressure increases everywhere monotonically with increasing viscosity ratio reaching a maximum before subsequently decreasing, and of [26] who considered the inverse problem of determining the required channel geometry to obtain a desired liquid-liquid interface profile.

Compared to the case of gravity-driven single layer films flowing down an inclined plane, their bilayer counterpart can prove to be unstable, even in the absence of inertia, due to the liquid-liquid interface present and triggered by the discontinuity in the fluid properties across it. Sometimes referred to as an inertialess instability, it was first identified by [27], when studying single layers, and as being related to the presence of a solid boundary close to the associated liquid-gas interface. Kao [28, 29] was the first to investigate the stability of gravity-driven bilayer thin films, for liquids having different viscosity, density and thickness, using the approach adopted by [30]. Two modes of instability were identified: an interface and a free-surface mode. It was also shown that when the lower layer is less viscous than the upper one the flow becomes unstable, even at $Re = 0$. Loewenherz and Lawrence [31] further investigated

the inertialess instability focussing on the influence of viscosity stratification, assuming both liquids to have the same density, and arrived at the same conclusion. Subsequently, [32] showed that instability can arise at any Reynolds number and/or upper layer surface and liquid-liquid interfacial tension. Hu et al. [33] found, as expected, that when the upper layer is heavier, the flow is always unstable; [34] subsequently extended these findings to the nonzero Reynolds number case while [35] included the effect of wall deformability on the interfacial instability of gravity-driven flow for two superposed Newtonian liquid layers.

More generally but related to the present investigation, [36] explored steady gravity-driven bilayer thin film flow emerging from a channel and flowing down an inclined flat substrate. The density of each layer was assumed to be the same, while viscosity and the surface and interfacial tension were taken as being different. Using the model of [37], with an assumed semi-parabolic velocity profile, they found that the surface-to-interfacial tension ratio, viscosity ratio and layer thickness ratio significantly affect the free surface and interface profiles.

The current paper explores the similarities and differences between steady bilayer channel and free-surface gravity-driven flow over locally specified step-up/-down and trench/peak like topographical features using a model based on the long-wave approximation and derived in the general sense for a system of n-layers. Section 2 introduces the flow configurations of interest, details the mathematical formulation together with further simplifications based on a depth-averaging approach and describes the associated method of solution. A comprehensive set of results is presented and analysed in section 3 with comparisons drawn to the work of others; finally, conclusions concerning the body of work are provided in section 4, together with suggestions for future investigation.

2. Mathematical Model and Solution Methodology

Although the current focus is continuous bilayer flow, rather than restrict the formulation of the governing equation set to just two layers, the more general case for n-layers is rigorously derived. The liquid layers are assumed to be Newtonian and incompressible with constant density, $\hat{\rho}_i$, dynamic viscosity, $\hat{\mu}_i$, and surface tension, $\hat{\sigma}_i$, where the subscript $i = 1, 2....n$ denotes the layer number from the bottom-most to top-most. In addition, the liquids are assumed to be immiscible which, although a reasonable approximation from a modelling perspective, may not always be the case encountered in practice. To simplify the problem further the selection of appropriate scalings is important in order to obtain a consistent set of non-dimensional equations of motion and continuity, that capture the key features of the flow. To this end the in-plane length scale, L_0, is taken as being proportional to the capillary length; the normal scale, H_0, is either the inlet thickness of the channel or the undisturbed total height of the contiguous layers in the case of free-surface flow; the pressure scale is $P_0 = \hat{\mu}_1 U_0 L_0 / H_0^2$, the time scale $T_0 = L_0/U_0$ and the velocity scale U_0 as provided in Appendix A.

The two-dimensional domains of interest are defined by a Cartesian coordinate system (x, z); the positive x-axis is in the flow direction and the positive z-axis normal to it; the non-dimensional time is denoted by t and inclination angle to the horizontal by θ. For illustrative

purposes, Figure 1 provides cross-sectional, two-dimensional, schematic diagrams for the two flow configurations explored; CON1 and CON2, for channel and free-surface flow, respectively – restricted to the case of two layers for the sake of clarity.

The disparity between the in-plane and normal length scales in the form of the small long-wave ratio $\varepsilon = H_0/L_0 << 1$, which in turn results in the ratio of the corresponding z- and x-velocity (W_0 and U_0) scales being similarly small $W_0/U_0 = \varepsilon << 1$, can be exploited advantageously, [38]. In that the scaled governing Navier-Stokes equations can be simplified considerably by ignoring terms of order $O(\varepsilon^2)$, reducing the dimensionality by one and making the problem more tractable computationally. Accordingly, the non-dimensional equations of motion and continuity for layer-i forming a sequence of n-layers reduce to:

$$\varepsilon\rho_i Re\left(\frac{\partial u_i}{\partial t} + u_i\frac{\partial u_i}{\partial x} + w_i\frac{\partial u_i}{\partial z}\right) = -\frac{\partial p_i}{\partial x} + \mu_i\frac{\partial^2 u_i}{\partial z^2} + \rho_i B\sin\theta, \tag{1}$$

$$\frac{\partial p_i}{\partial z} + \rho_i B\varepsilon\cos\theta = 0, \tag{2}$$

$$\frac{\partial u_i}{\partial x} + \frac{\partial w_i}{\partial z} = 0, \tag{3}$$

where $u_i(x,z,t)$, $w_i(x,z,t)$ are the non-dimensional velocity components in the $x-$ and z-direction, respectively, $p_i(x,z,t)$ is the non-dimensional pressure, $\rho_i = \frac{\hat{\rho}_i}{\hat{\rho}_1}$ and $\mu_i = \frac{\hat{\mu}_i}{\hat{\mu}_1}$, the ratio of fluid properties in layer-i to their counterparts in the bottom-most layer; $Re = \dfrac{\hat{\rho}_1 U_0 H_0}{\hat{\mu_1}}$ is the Reynolds number (ratio of inertia to viscous forces), $B = \dfrac{\hat{\rho}_1 g H_0^2}{\hat{\mu}_1 U_0}$ is the gravity parameter (ratio of gravity to viscous forces) and g is the standard gravity constant.

The upper and lower interfaces bounding layer-i are located at $z = f_i(x,t)$ and $z = f_{i-i}(x,t)$, respectively; its corresponding thickness is $h_i(x,t) = f_i(x,t) - f_{i-i}(x,t)$ and there is a total of $(n+1)$ interfaces, f_i, $i = 0, 1..n$. For both flow configurations, the lower interface of the bottom-most layer, f_0, is a stationary rigid, planar surface that contains a topographical feature of length l_t and depth/height s_0, and generally defined by the function $f_0(x) = s(x)$, which has a non-zero value at the topography and zero elsewhere. For CON2 the upper interface of the top-most layer, f_n, is a free surface, while for CON1 it is a rigid planar surface, $f_n(x,t) = 1$, which can be either stationary or moving with a constant speed u_t in the x-direction.

The problem specification is completed via imposition of appropriate initial and boundary conditions. Initially, the interface separating each liquid layer, and the free surface in the case of CON2, can be taken to be flat:

$$h_i|_{t=0} = \begin{cases} h_{i0} - s, & i = 1, \\ h_{i0}, & i = 2, 3..n, \end{cases} \tag{4}$$

where h_{i0} denotes the undisturbed uniform thickness of layer-i. Note that $\sum_{i=1}^{n} h_{i0} = 1$, because the overall channel thickness or the undisturbed total asymptotic film thickness for free-surface flow is used as the normal scale.

The inlet, $x = 0$, is considered to be far enough away from a topographical feature such

that the flow is unidirectional there, while the liquid-liquid interfaces, and in the case of film flow the free surface, are flat:

$$u_i|_{x=0} = u_{i0}(z), \quad w_i|_{x=0} = 0, \quad h_i|_{x=0} = h_{i0}; \tag{5}$$

the velocity profile $u_{i0}(z)$ is derived as explained in Section 2.1.

Satisfaction of the kinematic and no-slip boundary condition at all internal liquid-liquid interfaces, $z = f_i$, $i = 0, 1..n$, requires that:

$$\frac{\partial f_i}{\partial t} + u_i|_{z=f_i}\frac{\partial f_i}{\partial x} - w_i|_{z=f_i} = 0, \tag{6}$$

$$u_i|_{z=f_i} = u_{i+1}|_{z=f_i}, \quad w_i|_{z=f_i} = w_{i+1}|_{z=f_i}. \tag{7}$$

Note that for both CON1 and CON2, the solid-liquid interface of the bottom-most layer, $z = f_0$, being a stationary rigid surface, requires that:

$$u_1|_{z=f_0} = w_1|_{z=f_0} = 0. \tag{8}$$

In the case of CON1 only, the upper interface of the top-most layer, $z = f_n$, is also a rigid surface which, without loss of generality, is taken to be moving such that:

$$u_n|_{z=f_n} = u_t, \quad w_n|_{z=f_n} = 0, \tag{9}$$

there; the limiting case of the upper rigid surface at rest being $u_t = 0$.

Finally, balancing of tangential and normal stresses at internal liquid-liquid interfaces, $z = f_i$, $i = 1, 2..n$ for CON2 and $i = 1, 2..n-1$ for CON1, requires:

$$\mu_i \frac{\partial u_i}{\partial z}|_{z=f_i} = \mu_{i+1}\frac{\partial u_{i+1}}{\partial z}|_{z=f_i}, \tag{10}$$

$$(p_i - p_{i+1})|_{z=f_i} = -\sigma_{i,i+1}\frac{\varepsilon^3}{Ca}\frac{\partial^2 f_i}{\partial x^2}, \tag{11}$$

where $Ca = \frac{\hat{\mu}_1 U_0}{\hat{\sigma}_1}$ is the capillary number (the ratio of viscous to surface tension forces), $\sigma_{i,i+1} = \left(\sqrt{\sigma_{i+1}} - \sqrt{\sigma_i}\right)^2$ is the interfacial tension, [39] and [40], and surface tension is scaled with that of the bottom-most layer counterpart, i.e. $\sigma_i = \frac{\hat{\sigma}_i}{\hat{\sigma}_1}$. For CON2 the upper interface of the top-most layer is in contact with air, thus the interfacial tension there is equal to the surface tension of the top-most liquid layer, $\sigma_{i,i+1} = \sigma_i$; the air is assumed to have constant ambient pressure, $p_{n+1} = p_A$, as well as negligible density and viscosity, i.e. $\rho_{n+1} = \mu_{n+1} = 0$.

For single layer flow, [12] derive the capillary length scale, L_0, as proportional to $\frac{H_0}{Ca^{\frac{1}{3}}}$ by balancing the capillary and pressure forces. Similarly, for multilayer flow, as discussed in [22], L_0 can be obtained from the normal stress balance, equation (11), being a function of the fluid properties and thicknesses of all the liquid layers. For simplicity, the expression of capillary length for single layer flow is adopted in the present work, which for consistency and, when necessary, comparison with the results of [22], [23] and [7], [14], is defined as $L_0 = \frac{H_0}{(3Ca)^{\frac{1}{3}}}$ and

$L_0 = \frac{H_0}{(6Ca)^{\frac{1}{3}}}$ for CON1 and CON2, respectively. While these relationships suggest that the long-wave approximation ($H_0/L_0 << 1$) is valid for small capillary numbers, $Ca << 1$, only, as demonstrated in [17] good quantitative agreement with corresponding full Navier-Stokes solutions can be achieved for values of s_0 up to 1.

2.1. Depth-averaged form (DAF)

Although the long-wave approximation reduces the complexity of the Navier-Stokes equations, further simplification still is required to generate numerical solutions to the problems of interest. A now common approach for this purpose is the integral-boundary-layer (IBL) approximation, characterised by the assumption of a parabolic velocity profile across the liquid layer, a method that can be traced back to [37, 41] who used it to investigate solitary waves in a thin viscous liquid layer on a uniform vertically aligned surface. Subsequently, different variants of the methodology have appeared and been employed by [42–46] to tackle different thin film flow problems. Alternatively, but akin to the IBL approach, depth-averaging the reduced Navier-Stokes and continuity equations, [47], is employed in the present work, with the feature that inertial effects are embodied as a matter of course. This depth-averaged form (DAF) is free from the zero Reynolds number limitation imposed by the lubrication approximation, but shares the same common restriction as the IBL method, in that the velocity across the film is assumed to have a self-similar quadratic profile.

Integrating the continuity equation (3) for layer-$i = 1, 2....n$ with respect to z from f_{i-1} to f_i, using Leibniz's rule and applying boundary conditions (6), leads to the following form of the mass conservation equation:

$$\frac{\partial h_i}{\partial t} + \frac{\partial \left(h_i \bar{u}_i\right)}{\partial x} = 0, \tag{12}$$

where $\bar{u}_i = \frac{1}{h_i}\int_{f_{i-1}}^{f_i} u_i dz$ is the depth-averaged x-velocity.

Integration of the w-momentum equation (2) for layer-$i = 1, 2..n$ (or $i = 1, 2....n-1$ for CON1) with respect to z from z to f_i and applying boundary condition (11) yields:

$$p_i - p_{i+1} = -\sigma_{i,i+1}\frac{\varepsilon^3}{Ca}\frac{\partial^2 f_i}{\partial x^2} + B\varepsilon\cos\theta\left(\rho_i - \rho_{i+1}\right)\left(f_i - z\right). \tag{13}$$

Similarly, integrating the u-momentum equation (1) for layer $i = 1, 2..n$ with respect to z from f_{i-1} to f_i, making use of Leibniz's rule, the continuity equation (3) and boundary conditions (6), gives:

$$\begin{array}{l} \rho_i \varepsilon Re\left\{\frac{\partial(h_i\bar{u}_i)}{\partial t} + \frac{\partial}{\partial x}\left[h_i\bar{u}_i^2 + \int_{f_{i-1}}^{f_i}(\bar{u}_i - u_i)^2 dz\right]\right\} = \\ = -h_i\frac{\partial p_i}{\partial x} + \mu_i\left(\frac{\partial u_i}{\partial z}|_{z=f_i} - \frac{\partial u_i}{\partial z}|_{z=f_{i-1}}\right) + \rho_i h_i B\sin\theta. \end{array} \tag{14}$$

Knowledge of the velocity profile within the liquid layers is required to determine the dispersion, $\int_{f_{i-1}}^{f_i}\left(\bar{u}_i - u_i\right)^2 dz$, and the friction, $\left.\frac{\partial u_i}{\partial z}\right|_{z=f_i}$, terms present in equation (14); it is obtained assuming lubrication like flow, i.e. the flow is slow enough that $Re \sim O(\varepsilon)$. In such cases the

left hand side of equation (1) can be set to zero, namely:

$$\frac{\partial^2 u_i}{\partial \xi_i^2} + A_i = 0, \tag{15}$$

where

$$\xi_i = \frac{z - f_{i-1}}{h_i}, \quad A_i = \frac{h_i^2}{\mu_i}\left(\rho_i B \sin\theta - \frac{\partial p_i}{\partial x}\right). \tag{16}$$

Equation (15) can now be integrated twice for layer-i with respect to ξ_i which, together with use of boundary conditions (7), leads to the following expression for the velocity profile across the layer:

$$u_i = 6\bar{u}_i\xi_i\left(1-\xi_i\right) + c_{i-1}\left(1-\xi_i\right)\left(1-3\xi_i\right) + c_i\xi_i\left(3\xi_i - 2\right), \tag{17}$$

written in terms of the average, $\bar{u}_i = \int_0^1 u_i d\xi_i$ and interfacial, $c_i = u_i|_{\xi_i=1} = u_{i+1}|_{\xi_{i+1}=0}$, x-velocities, which are related to A_i as follows:

$$\bar{u}_i = \frac{A_i}{12} + \frac{c_{i-1}}{2} + \frac{c_i}{2}. \tag{18}$$

The velocity profile (17) essentially assumes uni-directional flow based on a self-similar quadratic velocity profile. For flow over trench or peak topography, provided the feature is a simple configuration that does not give rise to a significant underlying eddy structure, this assumption has been shown to yield accurate solutions, [48]. The approach followed is that of [14] and [47] as used for single layer free-surface flow over topography and which produces excellent predictions when compared with experimental and other corresponding numerical results. Employing this velocity profile, the dispersion and friction terms are obtained as follows:

$$\int_{f_{i-1}}^{f_i}\left(\bar{u}_i - u_i\right)^2 dz = \frac{h_i}{5}\left(\bar{u}_i^2 - \bar{u}_i c_{i-1} - \bar{u}_i c_i + \frac{2}{3}c_{i-1}^2 + \frac{2}{3}c_i^2 - \frac{1}{3}c_{i-1}c_i\right), \tag{19}$$

$$\frac{\partial u_i}{\partial z}|_{z=f_i} - \frac{\partial u_i}{\partial z}|_{z=f_{i-1}} = \frac{6}{h_i}\left(c_{i-1} + c_i - 2\bar{u}_i\right). \tag{20}$$

Applying boundary conditions (8), (9) and (10) to the velocity profile (17) results in the following tridiagonal linear system of algebraic equations for the interfacial velocities:

$$\begin{cases} c_0 = 0, \\ m_i c_{i-1} + 2\left(m_i + m_{i+1}\right)c_i + m_{i+1}c_{i+1} = 3\left(m_i\bar{u}_i + m_{i+1}\bar{u}_{i+1}\right), \quad i = 1, 2..n-1, \\ c_{n-1} + 2c_n = 3\bar{u}_n \quad \text{CON2} \quad c_n = u_t \quad \text{CON1}, \end{cases} \tag{21}$$

where $m_i = \mu_i/h_i$. Solution of the tridiagonal matrix system (21) is readily obtained via Thomas's algorithm, [49]; for completeness, Appendix A provides illustrative examples for 1, 2 and 3 layers.

The $3n$ unknowns, $h_i, p_i, \bar{u}_i$, $i = 1, 2..n$ require $3n$ equations: for CON2 there are n equations from each of (12), (13) and (14), while for CON1 there are n equations from (12), (14), $n-1$

equations from (13) and 1 from the presence of a prescribed rigid upper surface:

$$\sum_{i=1}^{n} h_i = 1 - s. \tag{22}$$

The problem is closed by specifying the inflow condition at $x = 0$ and assuming fully developed flow far upstream and downstream of the topography:

$$h_i|_{x=0} = h_{i0}, \quad \bar{u}_i|_{x=0} = \bar{u}_{i0}, \qquad \left.\frac{\partial h_i}{\partial x}\right|_{x=l} = \left.\frac{\partial p_i}{\partial x}\right|_{x=0,l} = \left.\frac{\partial \bar{u}_i}{\partial x}\right|_{x=l} = 0, \tag{23}$$

where l is the length of the substrate and the inflow averaged velocities, $\bar{u}_{i0}$, are calculated by solving system (21) together with equation (18) as demonstrated in Appendix A.

Note that due to the rigid nature of the channel's bounding surfaces, equation (22), it follows that $\sum_{i=1}^{n} \frac{\partial h_i}{\partial t} = 0$; thus integrating the sum of the mass conservation equations with respect to x from $x = 0$ to x, gives:

$$\sum_{i=1}^{n} h_i \bar{u}_i = \sum_{i=1}^{n} h_{i0} \bar{u}_{i0} = q_0. \tag{24}$$

Accordingly, for flow in a channel the total flow-rate per unit width is constant, that is q_0.

Note also that for steady flow the mass conservation equations for each layer-i, equation (12), can be integrated with respect to x from $x = 0$ to x, giving:

$$h_i \bar{u}_i = h_{i0} \bar{u}_{i0} = q_{i0}; \tag{25}$$

hence in the case of steady flow (for both CON1 and CON2) the flow rate per unit width in each layer is constant, that is q_{i0}. Consequently, the system of governing equations can alternatively be rewritten in terms of film thicknesses, h_i, only. This is achieved by subtracting the u-momentum equation for layer-$(i + 1)$ from that of layer-i, equation (14), followed by substitution of the pressure difference equations, (13), and averaged velocities $\bar{u}_i = q_{i0}/h_i$; see Appendix B.

2.2. Topography definition

Following previous authors (e.g. [50]; [11]; [12] and [14]), since the topography appears as a function in the governing equations, it is defined via arctangent functions. Accordingly, one-dimensional step-up/-down and rectangular trench/peak topographies are defined as follows:

$$s(x^*) = s_0 \left[\frac{1}{2} \pm \frac{1}{\pi} \tan^{-1}\left(\frac{x^*}{\delta}\right)\right], \tag{26}$$

$$s(x^*) = \frac{s_0}{2 \tan^{-1} \frac{l_t}{2\delta}} \left[\tan^{-1}\left(\frac{x^* + l_t/2}{\delta}\right) - \tan^{-1}\left(\frac{x^* - l_t/2}{\delta}\right)\right], \tag{27}$$

where the coordinate system x^* has its origin at the centre of the topography, $x^* = x - x_t$ and δ is an adjustable parameter which is used to specify the steepness of the side(s) of a topography. Note that for CON1 with a step-down topography, in order to facilitate comparison with the

case of a step-up, the scale H_0 is defined as the thickness of the channel at outlet, $x = l$, rather than at inlet as stated above; accordingly, the inflow boundary condition (23) is also replaced with its outflow counterpart:

$$h_i|_{x=l} = h_{i0}, \quad \bar{u}_i|_{x=l} = \bar{u}_{i0}, \qquad \left.\frac{\partial h_i}{\partial x}\right|_{x=0} = \left.\frac{\partial p_i}{\partial x}\right|_{x=0,l} = \left.\frac{\partial \bar{u}_i}{\partial x}\right|_{x=0} = 0. \tag{28}$$

2.3. Method of solution

The unsteady DAF equations (12), (13) and (14), subject to the attendant boundary conditions, are solved numerically, using a second-order accurate finite difference scheme on a computational domain, $x \in [0, l]$, subdivided into n_p staggered grid points and locations for the different variables, see [51], but also with reference to thin film problems as described in detail in [47, 52]. The pressure and layer thickness are stored at points in between those of the averaged velocities. This arrangement is used as a remedy for the well-known checkerboard instability which arises when the first derivative of pressure and the terms in the continuity equation are calculated using central differencing when pressure and velocities are collocated, [53]. A staggered grid system allows differencing of the first order derivatives of pressure, that are specific to the DAF equations, to be calculated using two adjacent nodes rather than two alternate ones as would be the case if a collocated mesh is used, [54]. Temporal discretisation is performed using a fully explicit second-order predictor technique and an implicit β-method, see [55], with β taken to be 3/4; this value provides a balance between accuracy and stability as discussed in [47]. An automatic adaptive time-stepping scheme is incorporated into the solution strategy to optimise the time step selection in order to reduce the computational resource requirements. The time-stepping procedure adopted uses the local truncation error estimates (LTEs) obtained from the difference between predictor and corrector stages. Dirichlet boundary conditions are assigned as exact values at the boundary points, whereas Neumann ones are implemented by employing ghost nodes at the edge of the computational domain. The principal overall solution strategy is based on a combination Full Approximation Storage (FAS) and Full Multigrid methodology, as described in [14, 56], having been employed successfully to solve several thin film flow problems, [57], [47] and [58], and shown to be accurate, efficient and robust.

The solutions presented in Section 3, start from the initial condition of a flat free surface and liquid-liquid interface, together with a fully developed averaged velocity. A typical time step tolerance of $TOL = 10^{-3}$ was used to adjust the magnitude of the time increment. A computational domain of $l = 100$ is found to be sufficient to ensure fully developed flow far upstream and downstream of the topography for both flow configurations. In addition, with the focus being on bilayer flow, to ensure the mesh independence of the results generated, numerical experiments were performed using different numbers of grid points for reference cases of channel and film flow, with a step-down topography present, as a bench-mark. For convenience the liquid properties of both layers were taken to be the same and to have the same thickness, and $|s_0|$ taken to be 0.1 and 0.4. The percentage change in the capillary ridge height that formed upstream of the topography for each solution was plotted against the number of

mesh points employed, revealing a solution domain containing $n_p = 1025$ equally spaced mesh points on the finest level of a multigrid hierarchy to be more than sufficient to guarantee mesh independent results. Multigrid V-cycles with 5 grid levels were performed at each time step to reduce residuals below 10^{-5} on the finest grid level. Note too, the topography steepness parameter is set to 0.001, which in addition ensures solutions independent of δ, [14, 47].

3. Results and Discussion

The equations set and method of solution described in Section 2 enables an in-depth investigation to be performed of the two flow configurations of interest. As an aid to revealing the effect of different topography, fluid properties, inertia and layer thickness ratio:

(i) In the main the figures provided do not show the entire solution domain but focus instead on regions where there is significant free-surface and liquid-liquid interface disturbances present to be of interest.

(ii) The liquid-liquid interface profile for flow over a step-down topography is characterised by the presence of a capillary ridge upstream of the step while for flow over a step-up the interface profile exhibits an upstream capillary trough. The height(depth) of the capillary ridge(trough), $h_{ridge}(h_{trough})$, is defined/calculated as the difference between the maximum(minimum) interface height and the reference inlet interface height where the interface is flat. The same definition/calculation applies to the corresponding free surface capillary ridge and trough disturbances that arise in the bilayer film flow case.

3.1. Bilayer Channel flow: CON1

The flow depicted schematically in Figure 1(a), is explored first, the main focus being the influence of inertia and the properties of the upper liquid layer relative to the those of the lower one – in particular the limiting cases when the upper layer is negligible compared to the lower one and when both layers have essentially the same properties, consistent with the investigations of [22] and [23] – in terms of the topography type. In addition to their investigations, the following scenarios are explored: CON1 when (i) $0 < \theta < 90^o$, (ii) $\theta = 0$ and the flow is driven by a translating upper channel surface imparting a shearing motion to the adjacent liquid layer and effectively mimicking what might occur in, for example, a multi-layer slot coating device. The gravity parameter $B = \dfrac{\hat{\rho}_1 g H_0^2}{\hat{\mu}_1 U_0}$ is calculated using velocity scale U_0 (see Appendix A), the long-wave parameter ε is set to 0.1, the dimensionless interfacial tension $\sigma_{1,2} = 1$ and the capillary number $Ca = \epsilon^3/3 = 3.33 \times 10^{-4}$. In this way the chosen value of Ca ensures the model employed stays true to the underlying assumptions of the long-wave approximation and is effectively removed from the governing equations, appearing rather in the definition of the dimensional width of the topography which is measured in units of capillary length. In the case of step-up and step-down topographies it is completely removed from the analysis.

The Reynolds number range investigated is chosen to be in the stable region consistent with the findings of [59] so as to avoid the possibility of inertial instability. They investigated the gravity-driven flow of two superposed layers of immiscible Newtonian liquid in a inclined channel with planar side walls by extending the weighted residual approach proposed by [43] for single-layer flows and taking into account second order terms in the long-wave expansion. The work illustrates the complicated interaction between viscosity ratio and lower layer thickness in determining stability thresholds. Their analysis requires that for neutral stability the critical ratio $\left(\frac{\cot\theta}{Re}\right)_c$ is always much smaller than 1.0 except when h_{10}, the lower layer thickness, is close to unity. Accordingly, the inclination angle of the channel is taken to be $\theta = 10^\circ$ unless stated otherwise. The stable Reynolds number range based on this ratio is $Re \leq 150$. Note that the DAF is prone to greater error with increasing Re and/or $|s_0|$ that can be quantified by comparison with the corresponding N-S solutions and is reported for single layer gravity-driven film flow in [47].

3.1.1. Gravity-driven vertically aligned flow

As a benchmark, the channel flow problem considered by [22] for the case $Re = 0$ is solved, with step-down and peak topographical features compared; it is the former topographical feature that was used as part of the mesh independence study described in 2.3. Since the normal component of gravity is omitted from their governing lubrication equations the results they obtained are strictly correct for a channel that is vertically aligned only. Accordingly, the inclination angle is set to 90° for this particular comparison exercise.

Figure 2(a) shows the effect of increasing s_0 while keeping $h_{10} = 0.1$ for flow with a step-down topography when $\rho_2 = 0$ and $\mu_2 = 10^{-3}$, which [22] refer to as the single-layer limit because the effect of the upper layer is negligible; in their work, as here, the value of B is taken to be 12. Each curve in Figure 2(a) represents a particular value of s_0, starting at $s_0 = 0.04$ and increasing in intervals of 0.08 to the value 0.6; increasing s_0 leads to a monotonic increase in the capillary ridge height formed upstream of the step-down topography. This behaviour is similar to that experienced by a single layer thin film flowing down an inclined substrate over a similar step-down feature, [12], [7] and [14]. Generating results much beyond a step-height of $|s_0| = 0.6$ is compromised since the single-layer like behaviour of the flow leads to a capillary ridge with a value exceeding 1.0, noting that the upper rigid surface of the channel is located at $z = 1$.

Figure 2(b) considers the case when the top layer has the same properties as the bottom one, i.e. $\mu_2 = \rho_2 = 1$. By comparison, a non-negligible upper layer modifies the monotonic behaviour described above, in that the capillary ridge height first increases with increasing s_0 before decreasing as the gap between the interface and the bounding upper channel surface becomes smaller and smaller. This effect can be attributed to the large pressure gradient arising in the upper layer in order to drive the liquid through the narrow gap between the interface and the upper surface. The capillary ridge height is eventually completely suppressed at large s_0, as shown for the case when $|s_0| = 0.92$, with the presence of a non-negligible upper layer enabling solutions to be obtained for larger s_0 than in the single-layer limit.

Figure 3(a) shows the change of capillary ridge height with topography height for different combinations of ρ_2 and μ_2. Increasing the density or viscosity of the upper layer suppresses the capillary ridge and in all cases, except the single-layer limit, leads to a growth in capillary ridge height with topography height, which reaches a maximum before subsequently decreasing. Figure 3(b) reveals the dependence of the capillary ridge on the height of the step-down for several values of h_{10} when $\rho_2 = \mu_2 = 1$. Each curve shows the same trend for capillary ridge height, that of increasing to a maximum value with increasing s_0 followed by a reduction as s_0 is increased further still. It can be seen that the capillary ridge height is suppressed by increasing the thickness of the lower layer if $|s_0| < 0.65$; for a topography height, $|s_0|$, above this limit, the curves for different h_{10} intersect and the capillary ridge height can become negative. A negative value does not indicate transition from a ridge to a trough, simply that the interface position where the capillary ridge occurs is below the upstream reference interface thickness, h_{10}. The results displayed in Figures 2 and 3 are identical to those obtained by [22].

A direct comparison of the results generated here for $Re = 0$ with those of [22], is provided in Figure 4 for the case of flow in a channel containing a peak topography with $s_0 = 0.48$, widths l_t of 2 and 4, when $\rho_2 = \mu_2 = 1$; note that in this figure, and all those appearing subsequently, the x-axis is shifted so that the origin is located at the centre of the topography. It shows that when the topography is sufficiently wide enough the interface behaves as in the case of flow past two independent topographies; a step-up followed by a step-down.

3.1.2. Gravity-driven inclined flow

It is clear from the above that excellent agreement is obtained between the present model and method of solution and the predictions of [22], for the particular case $\theta = 90°$. When the channel is no longer vertical they will differ. This can be explained in terms of the normal gravity term in the pressure equation (13), $(\rho_2 - \rho_1)\varepsilon \cos\theta \dfrac{\partial(h_1 + s)}{\partial x}$, which does not appear in the [22]'s model formulation; being omitted from their derivation for simplicity. When $\rho_2 = \rho_1$ or the channel is vertical this term vanishes but the effect of ignoring it becomes significant when the inclination angle is small and the two liquids have different densities. Accordingly, [22]'s results are strictly applicable for vertically or nearly vertically aligned channels only, being quantitatively inaccurate for small inclination angles; Bertozzi and Brenner [60] arrived at the same conclusion when comparing theoretical predictions with experiments for film flow down an inclined plane. This is demonstrated in Figure 5 for flow through a channel with a step-down of $|s_0| = 0.1$, inclined at angles of $\theta = 5°$ and $10°$, with the case $\theta = 90°$ included as a comparison, when $h_{10} = 0.4, \rho_2 = 1 \times 10^{-3}$, $\mu_2 = 1$ and $B = \dfrac{12}{\sin\theta}$.

While the current focus is gravity-driven flow with zero applied pressure gradient, $\frac{\Delta p_i}{l} = 0$, when non-zero it arises in the u-momentum equation (14) as a contribution to the streamwise body force component, $\rho_i B \sin\theta - \frac{\Delta p_i}{l}$. Thus applying a negative pressure gradient effectively acts in the same way as an increase in inclination angle; for example, for the particular case of vertical flow $\theta = 90°$ and $\rho_2 = 1$ considered in [22] the gravity-driven interface profiles are strictly identical to those generated by a pressure gradient provided $\frac{\Delta p_i}{l} = -B = -12$.

Figures 6(a) and (c) show the interface profile generated for flow through a channel for

step-down values of $|s_0| = 0.1$ and 0.4, respectively, when the upper layer is effectively absent ($\rho_2 = 0, \mu_2 = 1\times10^{-3}$) and $h_{10} = 0.4$. They reveal that far from the topography the liquid-liquid interface and hence the thickness of the lower layer is unaffected as Re is increased from 0 to 150; it is approximately the same at the inlet and the outlet of the channel, i.e. $h_1|_{x=0} \approx h_{10}$, due to the absence of any influence from the upper layer. The figure also shows that with increasing Re the interface exhibits an increasingly more pronounced decaying upstream capillary wave profile in the vicinity of the topography, instead of a more-or-less single capillary ridge, as in the case when $Re = 0$. This behaviour finds support from the work of [61] and [16] for single layer free surface flow down vertically aligned substrate.

For step heights of 0.1 and 0.8, when the top layer is no longer negligible and has the same properties as the lower one, ($\rho_2 = \mu_2 = 1$), Figure 6(b) and (d), respectively, the resulting capillary wave at the liquid-liquid interface on the upstream side is suppressed; the thickness of the lower layer at inlet is smaller but has the same proportion as at the outlet, i.e. $h_1|_{x=0} = h_{10}\,(1 - |s_0|)$, which for step heights of 0.1 and 0.8 gives $h_1|_{x=0}$ a value of 0.36 and 0.08, respectively. It can be seen from Figure 6(d) that, for a step height of 0.8, increasing the Re number has negligible effect on the capillary wave, the effect being transferred to the flank of the interface on the downstream side producing a widening of the same.

With reference to Figure 6(e), it can be seen that in the single-layer limit the capillary ridge height increases monotonically with increasing Re or $|s_0|$; a point to note is that as the step-height becomes more significant, beyond $|s_0| = 0.3$, the capillary ridge begins to feel the presence of the upper channel surface with increasing Re because μ_2 is not exactly zero. A different trend is observed at the other limit when the fluid properties of both layers are the same, Figure 6(f). For each of the four Re values shown, the ridge height increases monotonically to reach a maximum with increasing $|s_0|$ before decreasing monotonically beyond a value of roughly $|s_0| = 0.45$; as noted by [22] in the case of zero inertia, and as observed in the figure, the ridge height becomes negative at large topography heights.

Inspection of the pressure gradients present in both layers, see Figure 7, provides useful insight as to the interface behaviour observed above. In the single-layer limit the pressure gradient is, as one can readily infer, zero in the upper layer; in the lower layer there is a pressure gradient predominantly in the vicinity of the topography but zero elsewhere. The pressure gradient reflects a strong Re number dependence; the magnitude of the pressure variations observed, including a peak corresponding to the presence of a capillary ridge followed by a deep negative minimum, are amplified as Re is increased. This explains the monotonic growth of the capillary ridge height with Re and $|s_0|$ and the constant value of the lower layer thickness when the interface is flat. For the case when the upper layer can no longer be considered negligible, the lower layer displays similar behaviour but with larger variations and a non-zero but negative pressure gradient in the narrow part of the channel; the upper layer now exhibits a pressure gradient, the magnitude of its variation increasing with increasing Re. As expected the pressure is higher in the wider part of the channel, i.e. the outlet, whereas in line with mass conservation, equation (25), the average speed is lower.

Figures 8(a-d) shows a sequence of interface profiles for flow in a channel with a step-down

topography for values of h_{10} from 0.1, in steps of 0.1, for the case of both a negligible and non-negligible upper layer and when $Re = 0$ and 150. As expected the single layer limit reveals the presence of a more pronounced capillary ridge, which is compounded as the Re number is increased. When both layers have the same fluid properties the effect is greatly reduced but the interface increasingly feels the presence of the upper surface of the channel the greater the value of h_{10}. The consequence of these plots is summarised more clearly in Figures 8(e-f). When $Re = 0$ it shows, for both scenarios, that there is a monotonic drop in the capillary ridge height with increasing h_{10}. This can be attributed to the fact that increasing h_{10}, while keeping $|s_0|$ constant, is equivalent to reducing the topography height which is known to reduce the capillary ridge height, [22] and [12]. Furthermore, for the none single-layer limit case this is accompanied by a larger pressure gradient in the top layer due to the increasing resistance to flow caused by reducing the gap between the interface and the upper channel surface.

When $Re = 150$ the trends are quite different. The two-layer case shows almost no change in the capillary ridge height with increasing interface height – what is observed is an almost imperceptible drop in the capillary ridge height in h_{10} going from 0.1 to 0.2 followed by an equally gradual increase until the point $h_{10} = 0.5$ is reached, following which it continues to decrease. In the single-layer limit the ridge height similarly decreases, but more so, when h_{10} is increased from 0.1 to 0.2, after which it grows quickly with increasing h_{10}. This can be attributed to the fact that the increased inertia of the lower layer in the single-layer limit faces no resistance from the top layer, while for the two-layer case the inertia of the top layer tends to suppress what is going on at the interface. This observation might also be a consequence of the fact that an essentially single layer flow at $Re = 150$ down a plane inclined at 10° to the horizontal would almost certainly be considered unstable according to established stability criteria. The effect on the interface profile of varying the density of the upper liquid layer is shown in Figure 9 with the impact on the trough upstream from the capillary ridge summarised in Figure 9(c). Increasing the density of the upper layer relative to the lower one reduces the capillary trough depth whether inertia is present or absent; in the former case the behaviour is nonlinear while in the latter it is more-or-less linear.

A step-up topography is also investigated, the results of which are shown in Figure 10. As in the case of the free-surface flow of a single liquid layer down an inclined substrate featuring a step-up, the interface profiles reveal a capillary trough upstream the topography. For both scenarios the effect of inertia is the same: a widening and amplification of the interface disturbances. Increasing the step height, $|s_0|$, or Reynolds number, Re, results in a monotonic increase in the depth of the capillary trough, regardless of the upper layer's properties, as illustrated in Figures 10(e) and (f). This behaviour is very different from that of the step-down discussed earlier; c.f. Figure 6. This can be related to the fact that the capillary trough, in contrast to the ridge associated with a step-down, does not impact on the flow of the upper layer and hence there is no excessive pressure build-up in the top layer in order to satisfy the mass balance.

In the context of rigour and for further validation purposes, the equations given in Appendix B where solved for the above problems using a methodology akin to the one used by [22] and

[23]. An additional aim being to resolve whether their failure to solve the channel flow problem with a step-up topography and $Re \neq 0$ was a consequence of the solver employed. In the present work this was achieved using the MA42 subroutine (a successor of MA32) from the Harwell Subroutine Library (HSL) which employs the frontal method variant of Gaussian elimination, [62]. The MA42 code solves a set of sparse linear equations by building a LU decomposition of the sparse matrix in order to avoid a large number of operations involving zero terms. The solution process for the steady-state equation set starts by performing forward elimination which is followed by a back-substitution step.

For the different channel cases examined above, step-up/-down and trench/peak topographies, when $Re \neq 0$, solutions obtained using either method where found to be indistinguishable from each other suggesting that the failure by [23] to solve the problem of bilayer channel flow over a step-up topography was not due the solver used; arguably and acknowledged by them, further investigation of the applicability of the diffuse-interface method they employed for this flow situation is required to determine the reason for the failure. Another possibility is their attempt to simulate flows at unrealistically high Reynolds numbers which according to the work of [59] are prone to inertial instability.

3.1.3. Shear driven horizontally aligned flow

It is possible to drive the flow by shearing the upper layer by moving the upper rigid surface of the channel at a constant speed, U_t, a requirement being that this layer is other than negligible; its fluid properties are thus taken to be $\rho_2 = \mu_2 = 1$. For a horizontally aligned channel, $\theta = 0$, and in the absence of an imposed pressure gradient, when the flow encounters a change in the channel height, due to the presence of a topographical feature, a pressure gradient is generated there; the flow in this region can be thought of as superposition of shear (Couette) flow and Poiseuille flow generated by an induced pressure gradient. Accordingly, a shearing speed of $U_t = \dfrac{\hat{\rho}_1 g H_0^2}{6\hat{\mu}_1}$ is applied to make sure the average speed (see Appendix A) in the channel is the same as in the case of the vertically aligned, $\theta = 90°$, gravity-driven flow considered above; from which it follows that $U_0 = \dfrac{U_t}{2}$ and $B = 12$.

Figure 11 shows the effect of inertia on shear-driven flow over a step-down of depth 0.1 and 0.8. The effect of increasing inertia, amplifying the capillary ridge and widening the disturbance, is more pronounced when $|s_0| = 0.1$. When $|s_0| = 0.8$ the capillary ridge effect is observed to be greatly reduced, the consequence being that the flank of the interface is more significantly affected; the insert, showing an exploded view, reveals that an increase in inertia can be sufficient to suppress the capillary ridge and associated trough almost completely as a consequence of the shearing action - a finding very different to the equivalent fixed upper surface case, Figure 6(d), in which the effect is smaller and the capillary ridge is suppressed by increasing inertia. Figure 11(c) and (d) shows in more detail the dependence of capillary ridge height for a fixed lower layer thickness and varying $|s_0|$ and fixed step depth for varying h_{10}, respectively, at Re values ranging from 0 to 150. The behaviour observed in Figure 11(c) is similar to that of Figure 6(f) but with the effect of Re more pronounced for $|s_0| > 0.4$; Figure 11(d) compares well with Figure 8(f) but in the case of shear driven flow both curves

are monotonically decreasing from $h_{10} = 0.1$ to 0.8 – the shear imparted to the flow overcomes the rise in capillary ridge height observed in going from $h_{10} = 0.1$ to 0.2 in the gravity-driven flow case.

3.2. Bilayer Film flow: CON2

Attention is now directed at the related problem of bilayer film flow as depicted schematically in Figure 1(b). The effect of inertia and the upper layer properties are explored for different topographies and comparisons drawn with complementary experimental results and numerical predictions from the literature. Due to the absence of an explicit inertial stability criteria for bilayer free-surface flow over topography and to avoid generating results in unstable flow regimes it was decided to use the inertial stability criterion for single-layer flow down an inclined substrate as a guide when determining the stable Reynolds number range to be explored. The well-known stability criterion for gravity-driven flow down inclined substrate requires the Reynolds number to be smaller than a certain critical value, Re_{crit}. The value of the critical Reynolds number depends on the inclination angle, θ, of the substrate, [63] and [30], and is given by:

$$R_{crit} = \frac{5}{4}\cot\theta. \tag{29}$$

When the density of the upper layer is smaller than that of the lower one, bilayer flow becomes more stable than its single layer counterpart while a heavier upper layer has a non-stabilising effect, [29]. Using the above criteria and setting $\rho_2 \leq 1$ ensures the flow is stable. It is clear from equation (29) that if the substrate is vertical the flow is unstable for all non-zero Re.

It is worth noting that expression (29) is arguably over restrictive, since recent research has shown that a surface with periodically repeating topography can have a beneficial effect, over its flat surface counterpart, on the critical Re at which there is an onset of instability – see for example [64–69] who show that for film flow over a wavy substrate islands of stability exist beyond the critical value given by equation (29). The same is demonstrated in the experiments of [7] for localised steep topography in which the Re involved was beyond the above strict analytically defined limit.

Due to the lack of numerical or experimental results in the literature for continuous bilayer flow over topography, the limiting case where both the lower and the upper liquids have the same properties is used as a test bed, in particular the experimental data of [7]. In order to make a direct comparison θ is set to 30° with the gravity parameter $B = \dfrac{\hat{\rho}_1 g H_0^2}{\hat{\mu}_1 U_0}$ which, using the velocity scale U_0 provided in Appendix A for the case when the upper layer has the same properties as the lower one, i.e. $\mu_2 = \rho_2 = 1$, gives $B = \dfrac{2}{\sin\theta}$ which in turn is in agreement with the single-layer case from [47]. The dimensionless interfacial tension at the internal liquid-liquid interface and the free surface (liquid-air interface) is taken to be $\sigma_{1,2} = 6.4 \times 10^{-4}$ and $\sigma_{2,3} = 1$, respectively.

Figure 12 shows the comparison for flow over step-up and step-down topographies with $|s_0| = 0.20$ when $\varepsilon = 0.128$, $Ca = \epsilon^3/6 = 3.50 \times 10^{-4}$ and $Re = 2.45$ and a spanwise trench with $|s_0| = 0.19$ and $l_t = 1.51$ when $\varepsilon = 0.132$, $Ca = 3.86 \times 10^{-4}$, $Re = 2.84$ (these quantities

are based on properties of water as per [7]: $\hat{\rho}_1 = 1000\ kg/m^3$, $\hat{\mu}_1 = 0.001\ Pa.s$ and $\hat{\sigma}_1 = 0.07\ N/m$). The origin is moved such that it is located at the centre of the topography and the free-surface location and topography profile are scaled with respect to the height/depth of the topography, namely $s^* = s/s_0$ and $f_2^* = (f_2 - 1)/s_0$, respectively. For the three cases shown the model accurately captures the key features of the disturbed free surface profile. These include the characteristic free-surface trough and capillary ridge just upstream of the step-up and step-down topographies, respectively, and the free-surface depression characteristic of flow over a trench, [14]. The plots reveal excellent agreement between the current numerical predictions and the experimental measurements for all three topographical features – indeed the r.m.s. deviation between the numerical and experimental results obtained for the free-surface profiles for all three spanwise topographies is within the experimental accuracy of 2% reported by [7].

The model enables exploration of the influence of the upper liquid layer properties as well as the height of the lower layer on the free surface and interface disturbance generated. The angle of inclination is set to $\theta = 10°$, $\varepsilon = 0.1$ and the capillary number to $Ca = \epsilon^3/6 = 1.167 \times 10^{-4}$. Figure 13 illustrates the influence of the upper layer density on the free surface disturbance for flow over topography when $Re = 0$. Three topographical features, a step-up, step-down and a trench with $l_t = 1.5$, are considered when $\mu_2 = 1$, $|s_0| = 0.2$ and $h_{10} = 0.5$. The investigations cover only the flow regimes when the presence of the upper layer has a stabilising effect (i.e $\rho_2 \leq 1$). The effect of decreasing ρ_2 from 1 to 0.1 on the free surface, Figure 13 left column, for step-up/down topography, is a slight increase in the depth/height of the capillary feature and to push it away from the topography side wall. The effect on the free surface is more pronounced for flow over trench topography where the depth of the depression, formed after the capillary ridge, is reduced by 23%.

The corresponding liquid-liquid interface profiles for the flow configurations mentioned above, scaled with respect to the height/depth of the topography as $f_1^* = (f_1 - h_{10})/s_0$, are shown in Figure 13, right column. For this figure, as in other subsequent plots, inserts showing exploded views of the interface profiles formed are provided. These show that what appear as "kinks" are in fact smooth changes and simply an artefact of the graphical scaling employed. In general, the interface exhibits a profile similar to that of the free surface. However, it also shows features similar to those for the gravity-driven channel interface profile discussed above and also reported by [22]. The step-down flow has a capillary ridge with its peak pushed below the reference inlet interface which was noted for bilayer channel flow at high $|s_0|$ as shown, for example, in Figure 2(b). The effect of changing density on the interface profile is smaller than the effect on the free surface.

Changing the inlet thickness of the lower layer, h_{10} will have an impact on the free surface disturbance when the two liquids are not the same. Increasing h_{10} when $\rho_2 < 1$ is expected to have the same effect as increasing ρ_2 while h_{10} remains constant because both lead to an increased flow rate. This is confirmed by comparing Figure 14(a), which shows the free surface and interface profile for flow over a trench for different h_{10} values when $\rho_2 = 0.5$ and $\mu_2 = 1$, with Figure 13(c) for flow over a trench at different ρ_2 values. The two figures show the same trend, namely that the depth of free surface depression is increased when either h_{10} or ρ_2 are

increased. The corresponding interface profile behaviour is shown in Figure 14(b) for the cases h_{10}= 0.2, 0.4 and 0.8. The profile when $h_{10} = 0.2$ is very similar to the free surface profile characteristic of the flow of a single-layer thin film over a wide trench, as described by [18] who used the boundary element (BE) method to study the Stokes flow of a thin liquid film over a one-dimensional trench and by [14] who used a finite element method and lubrication theory to solve the problem of thin film flow over topography. When $h_{10} = 0.8$ the interface profile becomes very similar to that of the free surface.

Next the effect of changing the upper layer viscosity is explored keeping $h_{10} = 0.5$ and $\rho_2 = 1.0$ fixed. Figure 15 shows the influence of μ_2 on the flow over step-down and trench topographies. It can be seen that for the step-down, decreasing μ_2 leads to widening of the capillary ridge at both the free surface and liquid-liquid interface and the movement of the associated peak upstream of the topography side wall. The flow over a trench shows in addition a considerable decrease in the depth of the free surface and liquid-liquid interface depression of 14% and 15%, respectively, when μ_2 is decreased from 5 to 0.5.

The results shown in Figures 13 and 15 for flow over a step-down topography are informative from the standpoint of multi-layer cascade/slide coating processes in which films are formed by fluid pumped through a sequence of die slots with the upper most layer running over of the next adjacent layer and so on, as captured for bilayer flow in the classical images of [70], see also [5]. They show quite clearly the importance of the slot exit geometry for avoiding the presence/occurrence of eddies that can entrap bubbles and debris, and result in streak line defects; the numerical solutions of the associated governing equations by [71, 72] confirm the same. Related to this is the Patent filed in 2001 by [73] which sets out the use of very thin low viscosity carrier layers as an improved means of applying multi-layers to a moving substrate using slide/cascade coating systems. Subsequent to this [74] reported an extensive experimental analysis of carrier layers for the same coating arrangement, discovering that the limit to forming a thin carrier layer is determined at the point of formation and dependent on whether the layers above invade the slot from which the carrier layer, the last in line, emerges.

It is clear that the bilayer flow explored here is not the same in that it involves two layers that are already formed meeting a topographical feature rather than the feature itself being part of the initial film forming process and the complexities that this entails. Nevertheless, what can be inferred from the current work, remembering that the density of the upper layer cannot be greater than that of the lower one, is that reducing the dynamic viscosity of the lower layer has roughly the same effect as increasing the density of the upper layer, on both the free surface and interface shapes. What the results show in relation to increasing the viscosity of the upper layer, by a factor of 10 (from 0.5 to 5.0) when $\rho_1 = \rho_2 = 1$, is that for flow over a step-down topography, Figure 15(a) and (b), both the free surface and interfacial disturbance due to the presence of topography is suppressed. While performing a detailed stability analysis is beyond the scope of the investigation carried out here it can plausibly be argued that changes to fluid properties which lead to a reduction in any free-surface and interfacial disturbances that arise must be advantageous with regard to potentially widening stable operating windows.

The model can be employed to illustrate the evolution of the interface from close to the

topography when the lower layer is infinitely thin up to the full extent of the film by changing h_{10}. This is demonstrated in Figure 16 for flow over a trench topography when $\mu_2 = \rho_2 = 1$ which essentially represents a single-layer flow; h_{10} takes values from 0.2 to 0.9 and is increased in increments of 0.1. These interface profiles effectively represent the streamlines of the flow as there is no flow across them.

The effect of inertia on both the free surface and liquid-liquid interface disturbance is now investigated further together with the influence of fluid properties, ρ_2 and μ_2. Figure 17 shows the free surface and interface disturbance generated for flow over trench topography, $l_t = 1.5$ and $|s_0| = 0.2$. Increasing Re widens and increases the amplitude of the free surface and interface disturbances. The free surface capillary ridge height, h_{ridge}, increases by 76% and the interface's by 84% when Re increases from 0 to 30. The same behaviour was noted for the single-layer limit of channel flow as discussed above and also agrees with the predictions of [47] for single-layer free-surface flow. The change of h_{ridge} with Re for different combinations of ρ_2 and μ_2 is shown in Figure 18. For all ρ_2-μ_2 combinations, increasing Re increases h_{ridge} monotonically due to the increased inertia. The wavy interface seen in the case of bilayer gravity-driven channel flow at high Re is not observed here as the range of Re is limited due to stability constraints.

4. Conclusions

Two related bilayer flow problems are investigated numerically: through a channel and over a plane, both featuring well defined localised topography and inclined at a prescribed angle to the horizontal. Invoking the long-wave approximation facilitates the derivation of a common reduced equation set, embodying Reynolds number effects, applicable to the general case of n-layers. Details of the underpinning flow structure is absent by virtue of the modelling approach adopted but care has been taken to ensure that the topographical features considered are consistent with those explored in related single layer film flow problems, for which reduced models and solutions based on the full Navier-Stokes equations have been shown conclusively to be in extremely good agreement, even beyond the strict limits imposed by the long wave approximation. In addition, in the limit when both layers have the same fluid properties the equivalent single layer solution is recovered exactly.

Comparison is made with the work of others where it exists in the literature, with the mesh independent results generated for interfacial and free surface shape, both unknown *a priori*, found to be in excellent agreement. Furthermore, prior to performing a systematic investigation of both flow configurations, the validity of the modelling and accompanying method of solution was established by investigating the vertically aligned channel flow problem considered by [22] when $Re = 0$. In all cases, for the same fluid properties and topography types, the results obtained are found to be indistinguishable.

Next, a detailed systematic investigation of the above problem with the channel inclined at an angle less than 90^o to the horizontal was performed by varying the topography height/depth, the liquid properties of the upper layer, the liquid-liquid interface height and the Reynolds

number. In their attempts to explore a related problem, [23], they were unable to obtain a solution for the case of a step-up topography, attributing this to the solver they employed. In order to confirm this or otherwise, a method of solution similar to the one used by them was employed to solve the steady-state version of the equation set derived here. No such difficulty was encountered in obtaining solutions for the case of a step-up, indicating their inability to achieve the same outcome arguably stems from a different source. Other means of driving flow in an channel have been considered, in particular shearing the flow for a channel in horizontal alignment which results in subtle differences compared to the gravity-driven case.

For the case of bilayer free surface film flow, first of all an assessment of the quality of the predictions obtained is made by comparing the results for the single-layer-equivalent limit obtained experimentally by [7] and the associated existing numerical solutions of [47]. For all three topographical features investigated there is found to be excellent agreement. The model was used subsequently in a systematic sense to explore parameter space, in a similar way to the channel flow problem, with and without inertia present. Increasing inertia is found to widen and enhance the amplitude of free surface and liquid-liquid interface disturbances. Lowering the density of the upper layer has a strong influence in the case of flow over a trench topography by producing a notable decrease in the free-surface depression, but less so in terms of the effect on the capillary trough/ridge for flow over step-up/-down topography, respectively, or for the capillary ridge for flow over a trench topography. For all three topography types, it is found that changing the liquid-liquid interface height leads to a similar effect; in the case of flow over a tench topography, changing the upper layer viscosity has an amplifying effect on both the free surface depression and the capillary ridge, while for a step-down topography it has a suppressing effect. For the latter, parallels are drawn with the process of cascade/slide coating and in particular the practice of using a low viscosity carrier layer to improve the deposition of multi-layer films onto moving substrate.

The methodology and investigations reported in this paper offer considerable scope for progessing the work along a number of different and complementary avenues. When deriving model equation sets based on depth averaging of the Navier-Stokes and Continuity equations it could well prove worthwhile to explore the use of weighted averaging rather than the standard averaging employed in the present work; the reason being that the weighted residual approach has been shown to lead to improved results in the context of determining the inertial stability limit for single layer film flow, see [43, 44]. In this context the model equations could be used to generate base solutions from which to explore the stability of multilayer gravity-driven free surface film flows. Similarly, a complementary investigation could be undertaken into the effect of non-Newtonian behaviour of the liquids, with either one or more layers being so described; this could be broadened to explore in more detail the carrier layer problem by widening the scope of viscosity and lower layer thickness difference. An obvious further extension of the work would be to the exploration of three-dimensional multilayer free-surface film flows encountering topography and from a stability perspective; the associated finite difference equations are well suited to, and would require, a fast, accurate and efficient method of solution based on a multigrid strategy in tandem with error-controlled automatic time-stepping of the sort described

in Section 2.3.

Last but not least, the lack of experimental data for bilayer film and, in particular, channel flow over topography represents a very worthwhile research opportunity in its own right, as a means of providing benchmark results for comparison with and the validation of theoretical investigations of the type reported here.

Acknowledgements

AAA gratefully acknowledges the financial support from the Libyan Ministry of Higher Education.

Appendix A. Interfacial velocities, boundary conditions for averaged velocities and velocity scale

Velocity scales and examples of the solution of the system of equations for the interfacial velocities, system (21), together with boundary boundary conditions for averaged velocities found using equation (18), and velocity scale U_0, for both channel and film flow.

Channel flow (CON1)

$U_0 = \frac{\hat{\rho}_1 g H_0^2}{\hat{\mu}_1 B}\frac{A_{10}}{12} + \frac{U_t}{2}$ (the average velocity for a single-layer flow).

Single layer flow (consistent with Couette flow with gravity and imposed pressure gradient, [75]):

$c_1 = u_t$, $\bar{u}_{10} = \frac{A_{10}}{12} + \frac{u_t}{2}$.

Bi-layer flow (consistent with [22]):

$c_1 = \frac{3m_1\bar{u}_1+3m_2\bar{u}_2-m_2u_t}{2m_1+2m_2}$, $\bar{u}_{10} = \frac{A_{10}}{12}\frac{4m_{10}+m_{20}}{m_{10}+m_{20}} + \frac{A_{20}}{4}\frac{m_{20}}{m_{10}+m_{20}} + \frac{u_t}{2}\frac{m_{20}}{m_{10}+m_{20}}$,

$c_2 = u_t$, $\bar{u}_{20} = \frac{A_{10}}{4}\frac{m_{10}}{m_{10}+m_{20}} + \frac{A_{20}}{12}\frac{m_{10}+4m_{20}}{m_{10}+m_{20}} + \frac{u_t}{2}\frac{m_{10}+2m_{20}}{m_{10}+m_{20}}$.

Tri-layer flow (consistent with [24]):

$c_1 = \frac{6m_1m_2\bar{u}_1+6m_1m_3\bar{u}_1+3m_2^2\bar{u}_2+6m_2m_3\bar{u}_2-3m_2m_3\bar{u}_3+m_2m_3u_t}{4m_1m_2+4m_1m_3+3m_2^2+4m_2m_3}$,

$\bar{u}_{10} = \frac{A_{10}}{12}\frac{4m_{10}m_{20}+4m_{10}m_{30}+m_{20}m_{30}}{m_{10}m_{20}+m_{10}m_{30}+m_{20}m_{30}} + \frac{A_{20}}{4}\frac{2m_{20}^2+m_{20}m_{30}}{m_{10}m_{20}+m_{10}m_{30}+m_{20}m_{30}} + \frac{A_{30}}{4}\frac{m_{20}m_{30}}{m_{10}m_{20}+m_{10}m_{30}+m_{20}m_{30}} + \frac{u_t}{2}\frac{m_{20}m_{30}}{m_{10}m_{20}+m_{10}m_{30}+m_{20}m_{30}}$,

$c_2 = \frac{6m_1m_2\bar{u}_2-3m_1m_2\bar{u}_1+6m_1m_3\bar{u}_3+3m_2^2\bar{u}_2+6m_2m_3\bar{u}_3-2m_1m_3u_t-2m_2m_3u_t}{4m_1m_2+4m_1m_3+3m_2^2+4m_2m_3}$,

$\bar{u}_{20} = \frac{A_{10}}{4}\frac{2m_{10}m_{20}+m_{10}m_{30}}{m_{10}m_{20}+m_{10}m_{30}+m_{20}m_{30}} + \frac{A_{20}}{12}\frac{4m_{10}m_{20}+m_{10}m_{30}+12m_{20}^2+4m_{20}m_{30}}{m_{10}m_{20}+m_{10}m_{30}+m_{20}m_{30}} + \frac{A_{30}}{4}\frac{m_{10}m_{30}+2m_{20}m_{30}}{m_{10}m_{20}+m_{10}m_{30}+m_{20}m_{30}} + \frac{u_t}{2}\frac{m_{10}m_{30}+2m_{20}m_{30}}{m_{10}m_{20}+m_{10}m_{30}+m_{20}m_{30}}$,

$c_3 = u_t$,

$\bar{u}_{30} = \frac{A_{10}}{4}\frac{m_{10}m_{20}}{m_{10}m_{20}+m_{10}m_{30}+m_{20}m_{30}} + \frac{A_{20}}{4}\frac{m_{10}m_{20}+m_{20}^2}{m_{10}m_{20}+m_{10}m_{30}+m_{20}m_{30}} + \frac{A_{30}}{12}\frac{m_{10}m_{20}+4m_{10}m_{30}+4m_{20}m_{30}}{m_{10}m_{20}+m_{10}m_{30}+m_{20}m_{30}} + \frac{u_t}{2}\frac{m_{10}m_{20}+2m_{10}m_{30}+2m_{20}m_{30}}{m_{10}m_{20}+m_{10}m_{30}+m_{20}m_{30}}$.

Where $m_{i0} = \frac{\mu_i}{h_{i0}}$, $A_{i0} = \frac{h_{i0}^2}{\mu_i}\left(\rho_i B\sin\theta - \frac{\Delta p}{l}\right)$; $\frac{\Delta p}{l}$ is the non-dimensional imposed pressure gradient and U_t the dimensional upper surface speed.

Free-surface film flow (CON2)

Single layer flow (consistent with Nusselt flow, [75]):

$U_0 = \frac{\hat{\rho}_1 g H_0^2}{\hat{\mu}_1 B}\frac{A_{10}}{2}$ (free-surface velocity), $c_1 = \frac{3\bar{u}_1}{2}$, $\bar{u}_{10} = \frac{A_{10}}{3}$.

Bi-layer flow:

$U_0 = \frac{\hat{\rho}_1 g H_0^2}{\hat{\mu}_1 B}\left(\frac{A_{10}}{2} + \frac{A_{20}}{2}\frac{m_{10}+2m_{20}}{m_{10}}\right)$ (free-surface velocity),

$c_1 = \frac{6m_1\bar{u}_1+3m_2\bar{u}_2}{4m_1+3m_2}$, $\bar{u}_{10} = \frac{A_{10}}{3} + \frac{A_{20}}{2}\frac{m_{20}}{m_{10}}$, $c_2 = \frac{6m_1\bar{u}_2+3m_2\bar{u}_2-3m_1\bar{u}_1}{4m_1+3m_2}$, $\bar{u}_{20} = \frac{A_{10}}{2} + \frac{A_{20}}{3}\frac{m_{10}+3m_{20}}{m_{10}}$.

Tri-layer flow:

$U_0 = \frac{\hat{\rho}_1 g H_0^2}{\hat{\mu}_1 B}\left(A_{10} + \frac{A_{20}}{2}\frac{m_{10}+3m_{20}}{m_{10}} + \frac{A_{30}}{2}\frac{m_{10}m_{20}+2m_{10}m_{30}+2m_{20}m_{30}}{m_{10}m_{20}}\right)$ (free-surface velocity),

$c_1 = \frac{12m_1m_2\bar{u}_1+9m_1m_3\bar{u}_1+6m_2^2\bar{u}_2+9m_2m_3\bar{u}_2-3m_2m_3\bar{u}_3}{8m_1m_2+6m_1m_3+6m_2^2+6m_2m_3}$, $\bar{u}_{10} = \frac{7A_{10}}{12} + \frac{3A_{20}}{4}\frac{m_{20}}{m_{10}} + \frac{A_{30}}{2}\frac{m_{30}}{m_{10}}$,

$c_2 = \frac{12m_1m_2\bar{u}_2+6m_1m_3\bar{u}_3+6m_2^2\bar{u}_2+6m_2m_3\bar{u}_3-6m_1m_2\bar{u}_1}{8m_1m_2+6m_1m_3+6m_2^2+6m_2m_3}$, $\bar{u}_{20} = A_{10} + \frac{A_{20}}{6}\frac{2m_{10}+9m_{20}}{m_{10}} + \frac{A_{30}}{2}\frac{m_{10}m_{30}+2m_{20}m_{30}}{m_{10}m_{20}}$,

$c_3 = \frac{12m_1m_2\bar{u}_3+3m_1m_2\bar{u}_1+6m_1m_3\bar{u}_3+9m_2^2\bar{u}_3+6m_2m_3\bar{u}_3-6m_1m_2\bar{u}_2-3m_2^2\bar{u}_2}{8m_1m_2+6m_1m_3+6m_2^2+6m_2m_3}$,

$\bar{u}_{30} = A_{10} + \frac{A_{20}}{2}\frac{m_{10}+3m_{20}}{m_{10}} + \frac{A_{30}}{3}\frac{m_{10}m_{20}+3m_{10}m_{30}+m_{20}m_{30}}{m_{10}m_{20}}$.

Appendix B. Governing equations for steady-state multilayer flow

The system of governing equations for layer thicknesses, h_i, where $i = 1, 2..n$ for CON2 and $i = 1, 2..n-1$ for CON1, for steady-state multilayer flow are:

$$\begin{aligned}
&\varepsilon Re \frac{\rho_i}{h_i}\frac{\partial}{\partial x}\left[\frac{6q_{i0}^2}{5h_i} + \frac{h_i}{5}\left(\frac{2}{3}c_{i-1}^2 + \frac{2}{3}c_i^2 - \frac{1}{3}c_{i-1}c_i - c_{i-1}\frac{q_{i0}}{h_i} - c_i\frac{q_{i0}}{h_i}\right)\right] - \frac{6\mu_i}{h_i^2}\left(c_{i-1} + c_i - 2\frac{q_{i0}}{h_i}\right) - \\
&-\varepsilon Re \frac{\rho_{i+1}}{h_{i+1}}\frac{\partial}{\partial x}\left[\frac{6q_{i+1,0}^2}{5h_{i+1}} + \frac{h_{i+1}}{5}\left(\frac{2}{3}c_i^2 + \frac{2}{3}c_{i+1}^2 - \frac{1}{3}c_ic_{i+1} - c_i\frac{q_{i+1,0}}{h_{i+1}} - c_{i+1}\frac{q_{i+1,0}}{h_{i+1}}\right)\right] + \\
&+\frac{6\mu_{i+1}}{h_{i+1}^2}\left(c_i + c_{i+1} - 2\frac{q_{i+1,0}}{h_{i+1}}\right) = \sigma_{i,i+1}\frac{\varepsilon^3}{Ca}\frac{\partial^3 f_i}{\partial x^3} + B\left(\rho_i - \rho_{i+1}\right)\left(\sin\theta - \varepsilon\cos\theta\frac{\partial f_i}{\partial x}\right).
\end{aligned} \tag{30}$$

Here interfacial velocities c_i are determined by solving system (21) where averaged velocities on the right-hand sides are set to $\bar{u}_i = q_{i0}/h_i$. Note that CON2 is completed via the conditions $\rho_{n+1} = \mu_{n+1} = 0$, while CON1 is completed via condition $\sum_{i=1}^{n} h_i = 1 - s$.

Figures

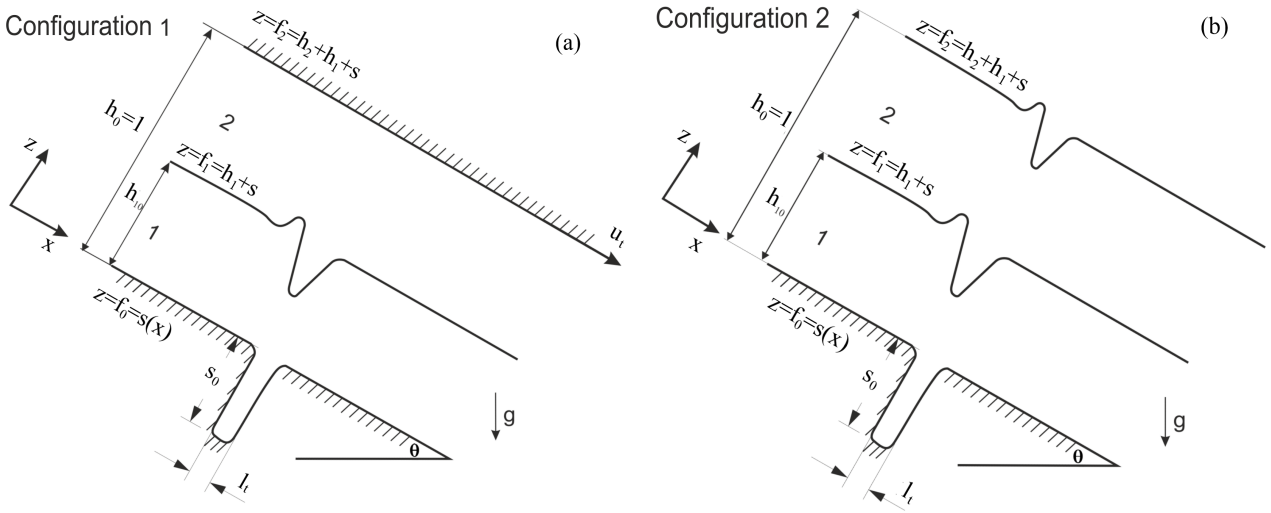

Figure 1: Schematic of two-dimensional gravity-driven bilayer flow through a channel (left), CON1, and down an inclined substrate (right), CON2, inclined at angle θ to the horizontal, showing the associated geometry and coordinate system for the problem, illustrated for flow past a trench-like topography.

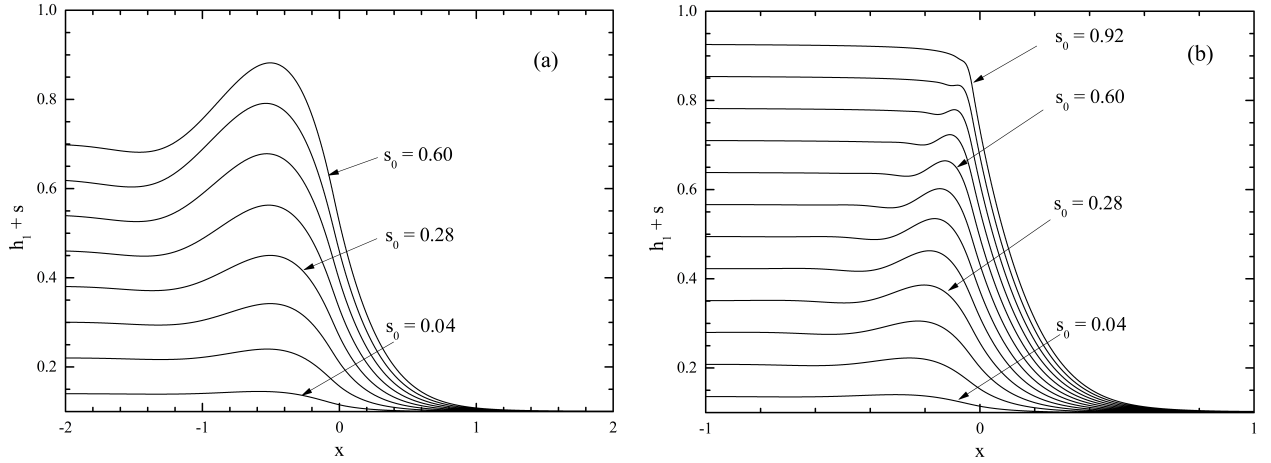

Figure 2: Effect of topography height on the interface profile for gravity-driven channel flow with a step-down topography when $h_{10} = 0.1, Ca = 3.33\times10^{-4}, \theta = 90°$. and $Re = 0$: (a) $\rho_2 = 0, \mu_2 = 1\times10^{-3}$; (b) $\rho_2 = 1, \mu_2 = 1$.

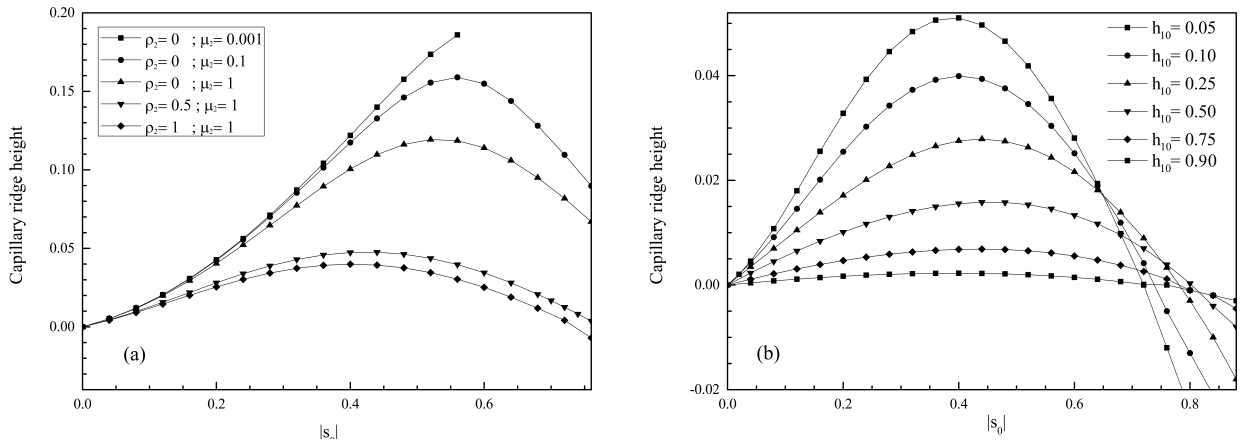

Figure 3: Effect of (a) liquid properties for $h_{10} = 0.1$ and (b) h_{10} for $\rho_2 = \mu_2 = 1$, on the capillary ridge height in terms of topography height for gravity-driven channel flow with a step-down: $Ca = 3.33 \times 10^{-4}$, $\theta = 90°$, $Re = 0$.

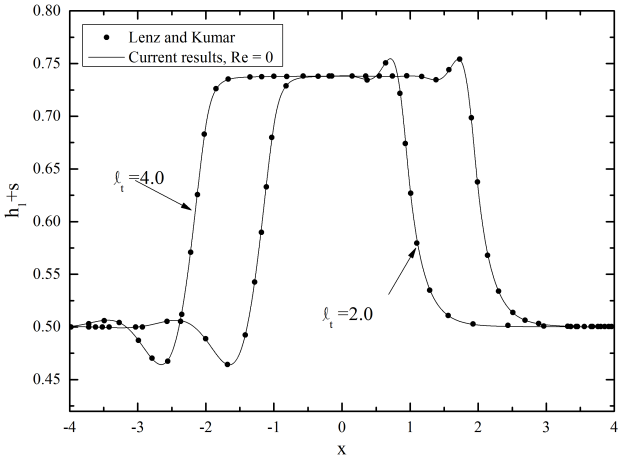

Figure 4: Comparison of current results with those of [22] for gravity-driven flow in channel containing a peak topography for the case $|s_0|$=0.48 when h_{10}=0.5, $Ca = 3.33 \times 10^{-4}$, $\rho_2 = \mu_2 = 1.0$, $\theta = 90°$, $Re = 0$.

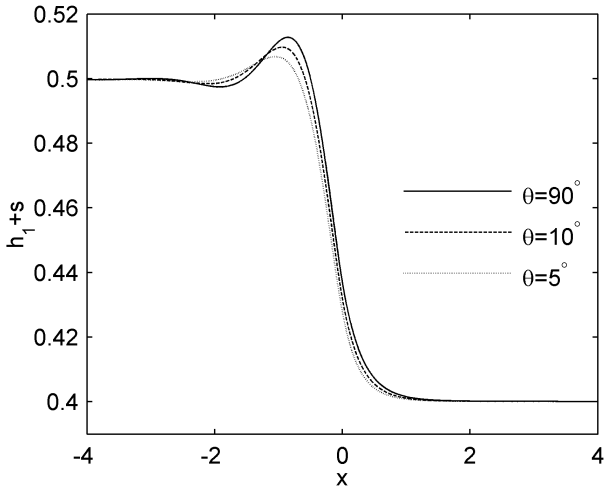

Figure 5: Effect of inclination angle, θ on interface shape for gravity-driven flow through a channel with a step-down of $|s_0| = 0.1$ when $h_{10} = 0.4$, $Ca = 3.33 \times 10^{-4}$, $\rho_2 = 1 \times 10^{-3}$, $\mu_2 = 1.0$, $Re = 0$.

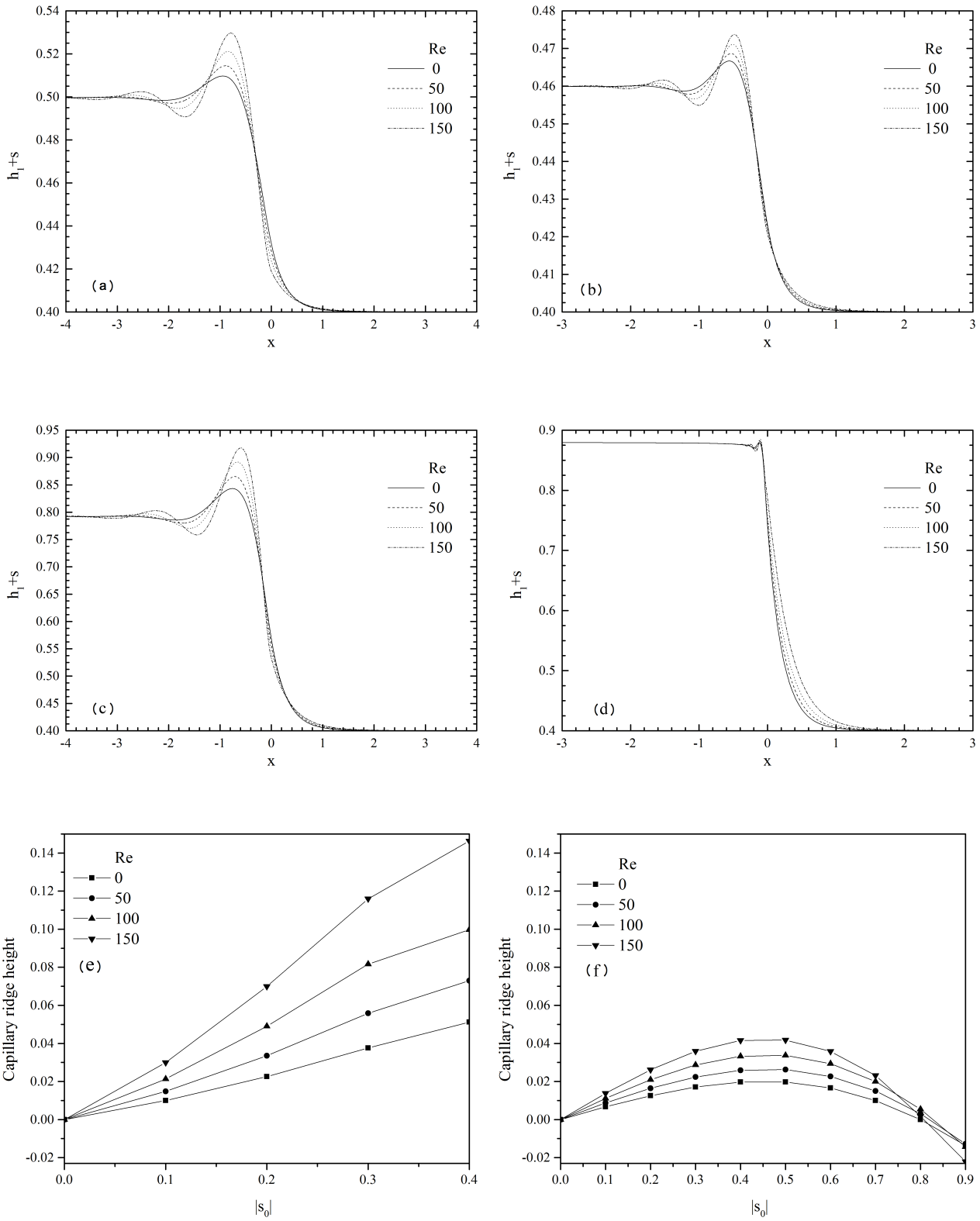

Figure 6: Interface profiles and capillary ridge height as a function of $|s_0|$ for gravity-driven flow in a channel containing a step-down topography in the absence and presence of inertial effects for $h_{10} = 0.4$, $Ca = 3.33\times10^{-4}$ and $\theta = 10°$: $\rho_2 = 0, \mu_2 = 1 \times 10^{-3}$ (left column), $\rho_2 = \mu_2 = 1.0$ (right column), $|s_0| = 0.1$ (top row), $|s_0| = 0.4$ (middle row left), $|s_0| = 0.8$ (middle row right), capillary ridge height (bottom row).

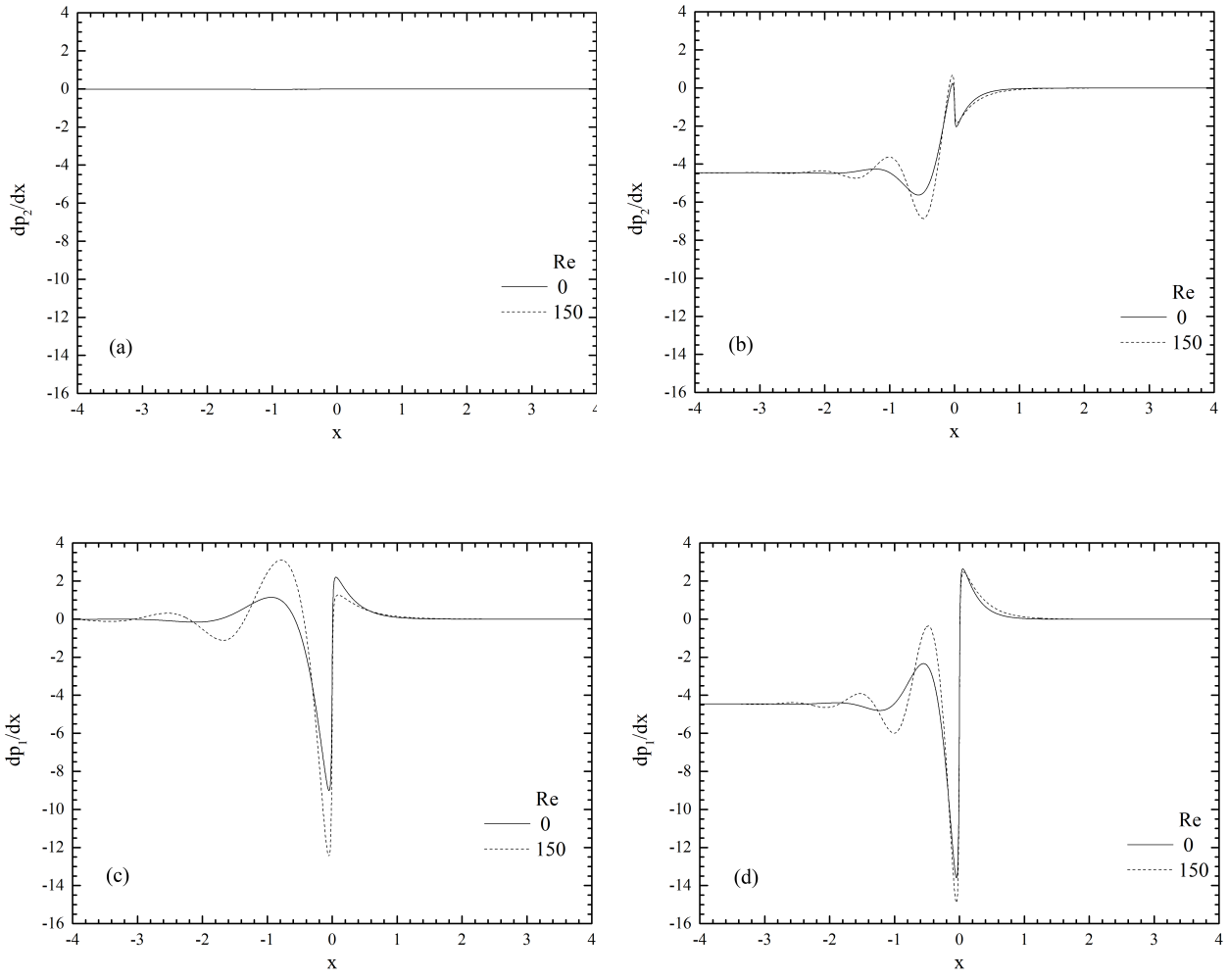

Figure 7: Pressure gradient profiles for gravity-driven flow in a channel containing a step-down of $|s_0| = 0.1$ when $h_{10} = 0.4$, $Ca = 3.33 \times 10^{-4}$, $\theta = 10°$, with: $\rho_2 = 0, \mu_2 = 1 \times 10^{-3}$ (left column), $\rho_2 = \mu_2 = 1.0$ (right column), upper layer (top row), lower layer (bottom row).

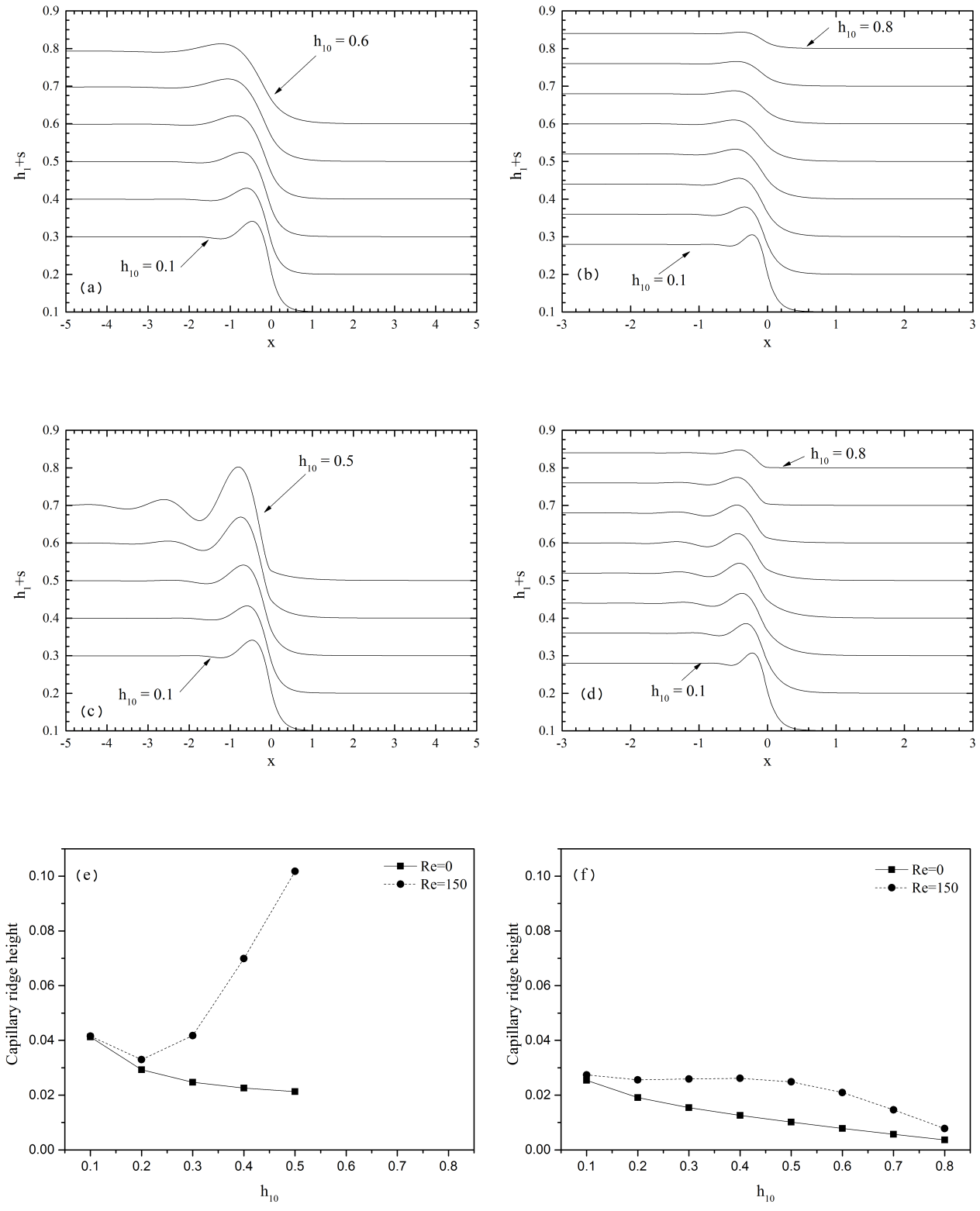

Figure 8: Effect of h_{10} on the interface shape and capillary ridge height for gravity-driven flow in a channel with a step-down of $|s_0| = 0.2$ in the absence and presence of inertial effects when, $Ca = 3.33 \times 10^{-4}$, $\theta = 10°$: $\rho_2 = 0, \mu_2 = 1 \times 10^{-3}$ (left column), $\rho_2 = \mu_2 = 1.0$ (right column), $Re = 0$ (top row), $Re = 150$ (middle row), capillary ridge height (bottom row).

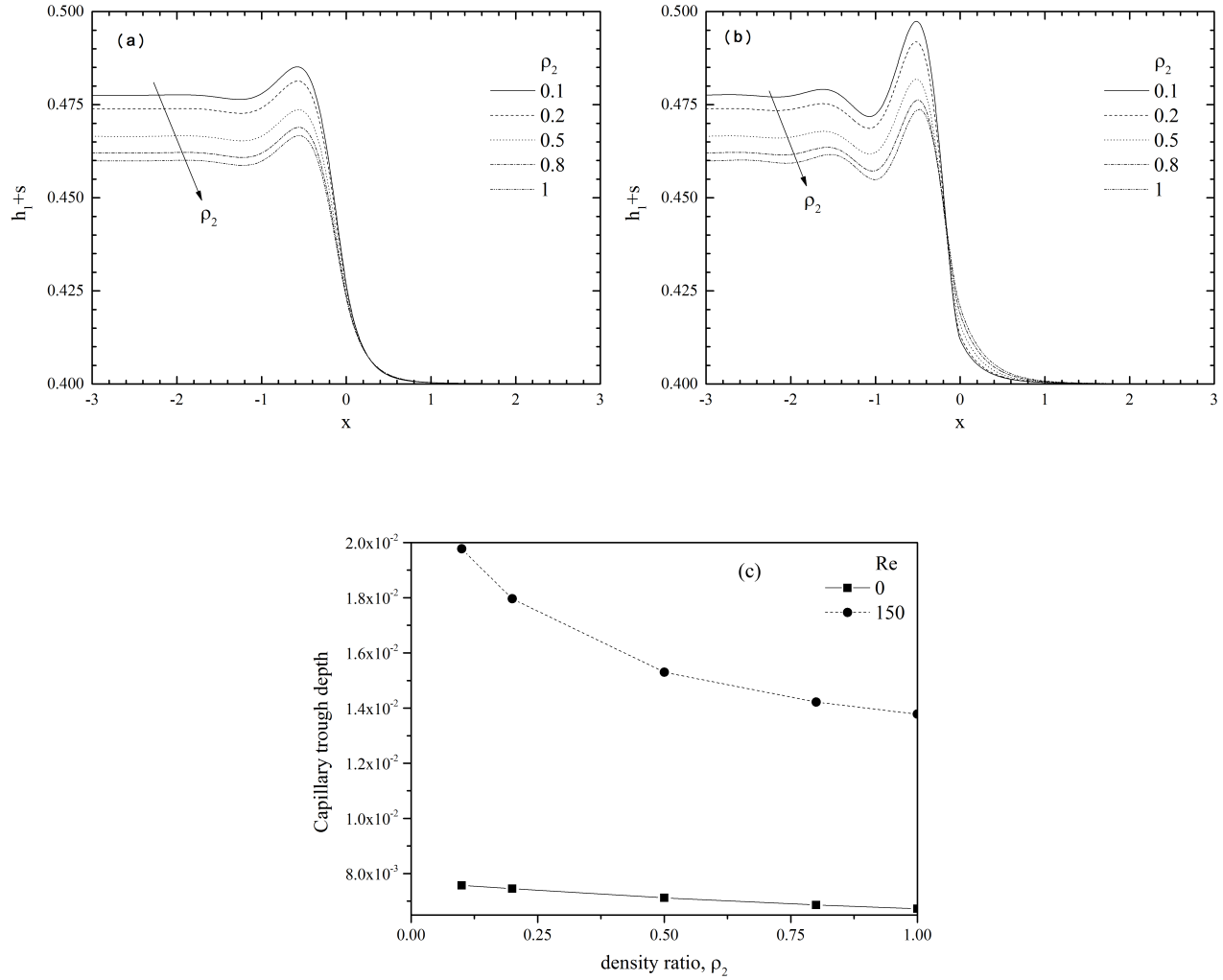

Figure 9: Effect of density ratio on the interface shape and capillary trough depth for gravity-driven flow in a channel with a step-down of $|s_0| = 0.2$ when h_{10}=0.4, $Ca = 3.33 \times 10^{-4}$ and $\mu_2 = 1.0$, $\theta = 10°$ for: (a) $Re = 0$; (b) $Re = 150$; (c) capillary trough depth as a function of ρ_2.

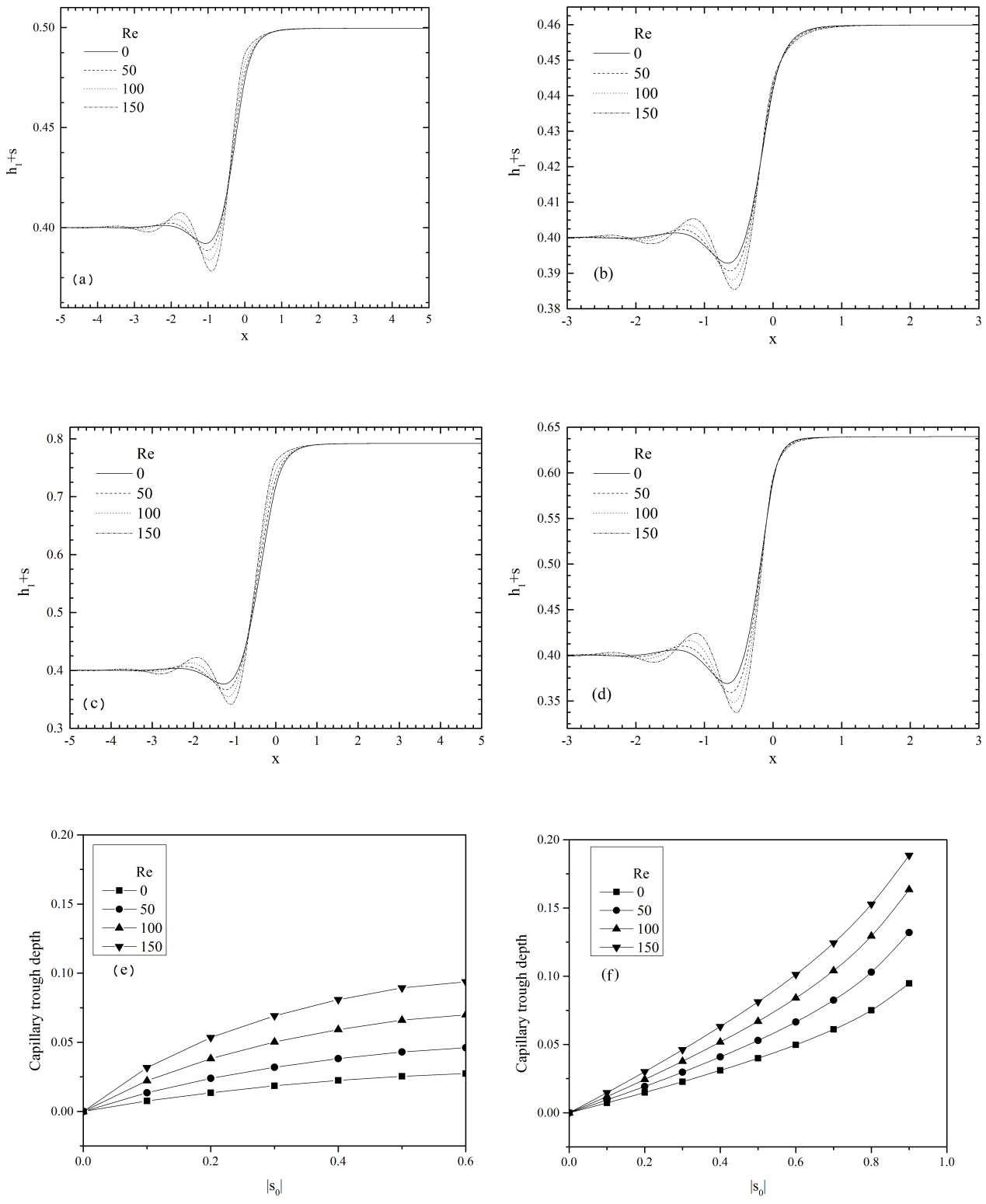

Figure 10: Interface profiles and capillary trough depth as a function of $|s_0|$ for gravity-driven flow in a channel containing a step-up topography in the absence and presence of inertial effects for $h_{10} = 0.4$, $Ca = 3.33 \times 10^{-4}$, $\theta = 10°$: $\rho_2 = 0, \mu_2 = 1 \times 10^{-3}$ (left column), $\rho_2 = \mu_2 = 1.0$ (right column), $|s_0| = 0.1$ (top row), $|s_0| = 0.4$ (middle row), capillary trough depth (bottom row).

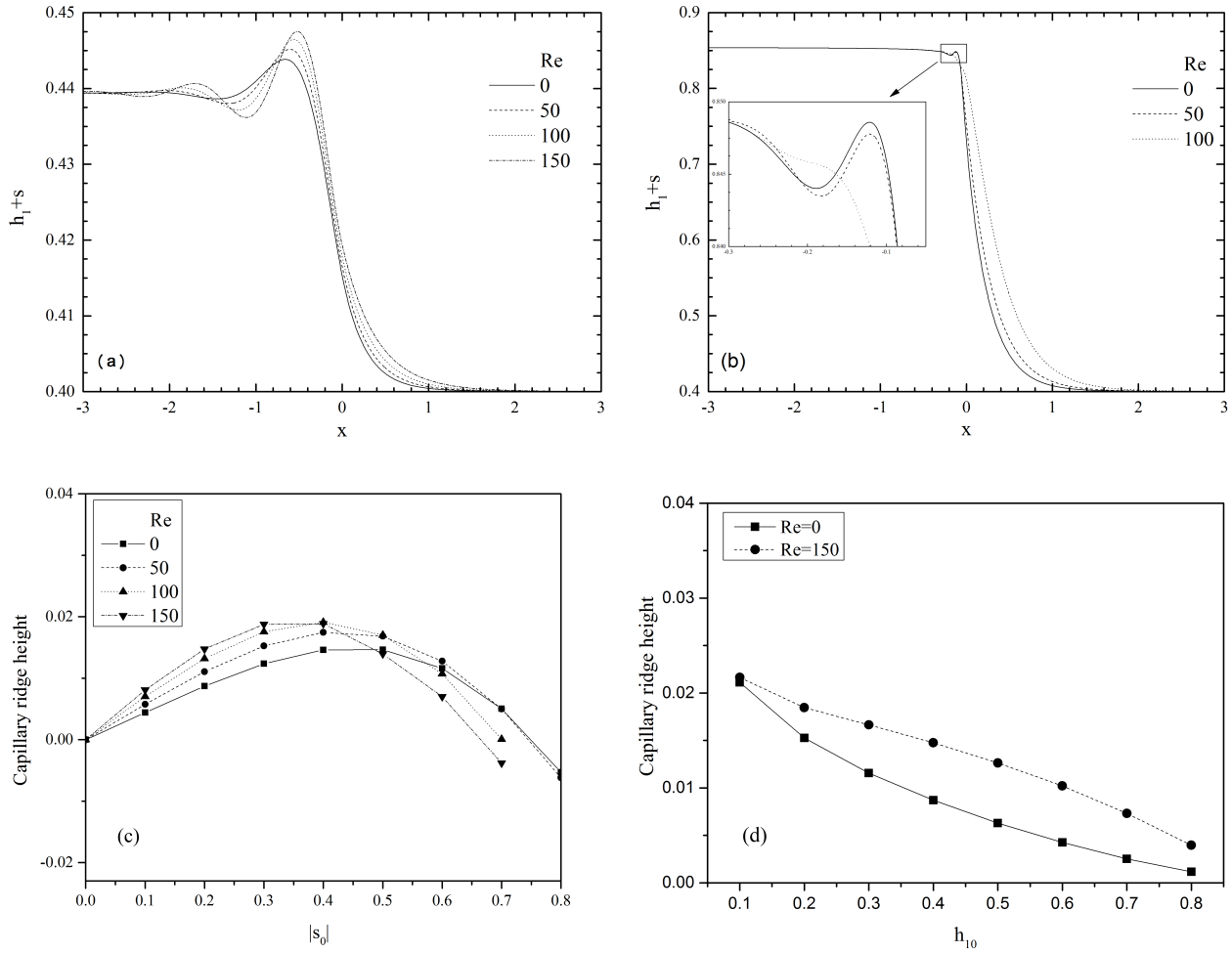

Figure 11: Interface profiles and capillary ridge height as a function of $|s_0|$ and h_{10} for shear-driven flow in a channel containing a step-down in the absence and presence of inertial effects when $Ca = 3.33 \times 10^{-4}$, $\theta = 0^\circ$ and $\rho_2 = \mu_2 = 1$: (a)h_{10}=0.4 and $|s_0| = 0.1$, (b)h_{10}=0.4 and $|s_0| = 0.8$, (c)$h_{10} = 0.4$ and (d)$|s_0| = 0.1$.

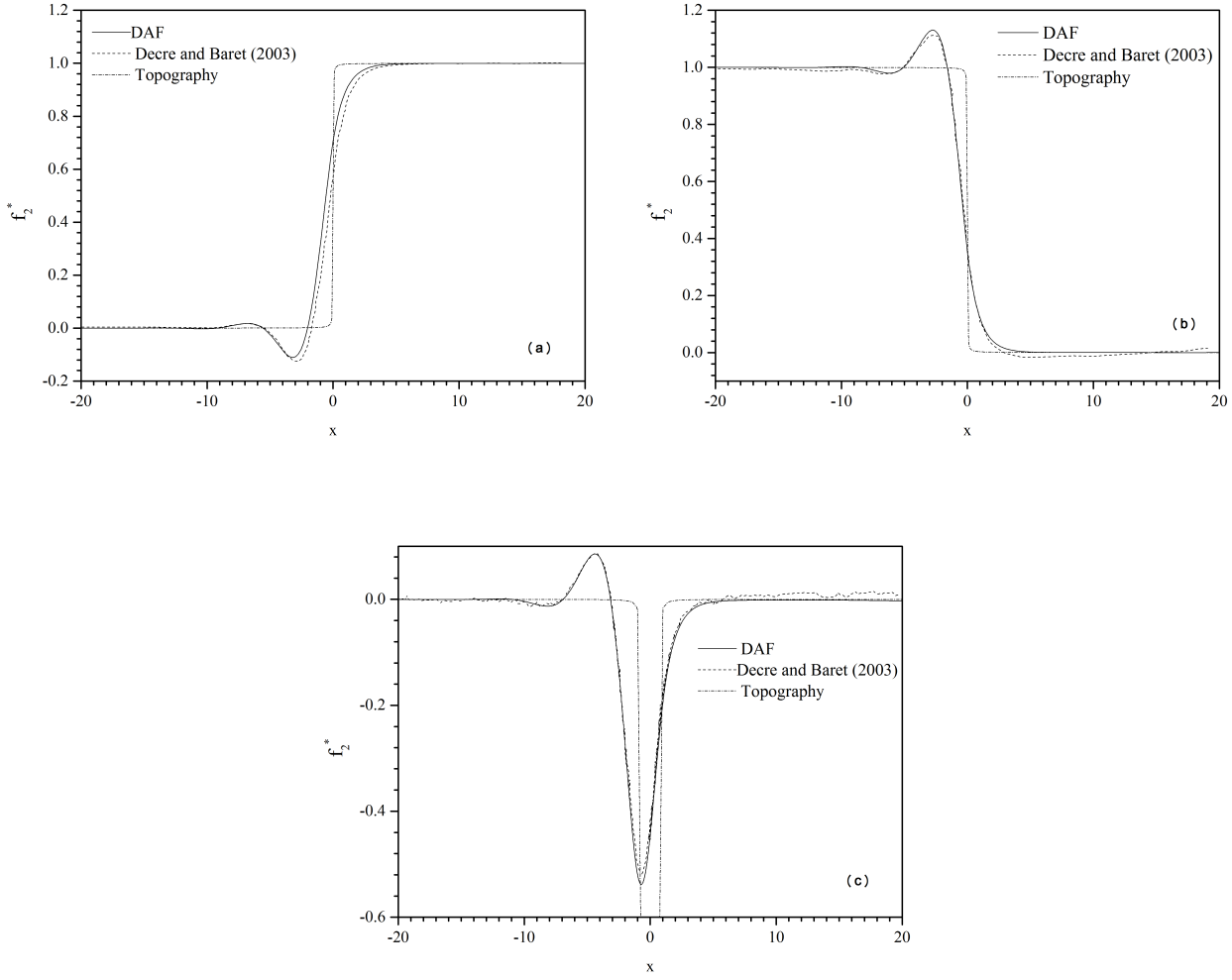

Figure 12: Comparison between DAF predictions of the free surface disturbance when $\rho_2 = \mu_2 = 1$ with the experimental results of [7] for gravity-driven film flow over a substrate containing topography with $\theta = 30°$: (a) step-up (height $|s_0| = 0.2$ and Re $= 2.45$); (b) step-down (depth $|s_0| = 0.2$ and Re $= 2.45$); (c) trench ($|s_0| = 0.19$, $l_t = 1.51$ and Re $= 2.84$).

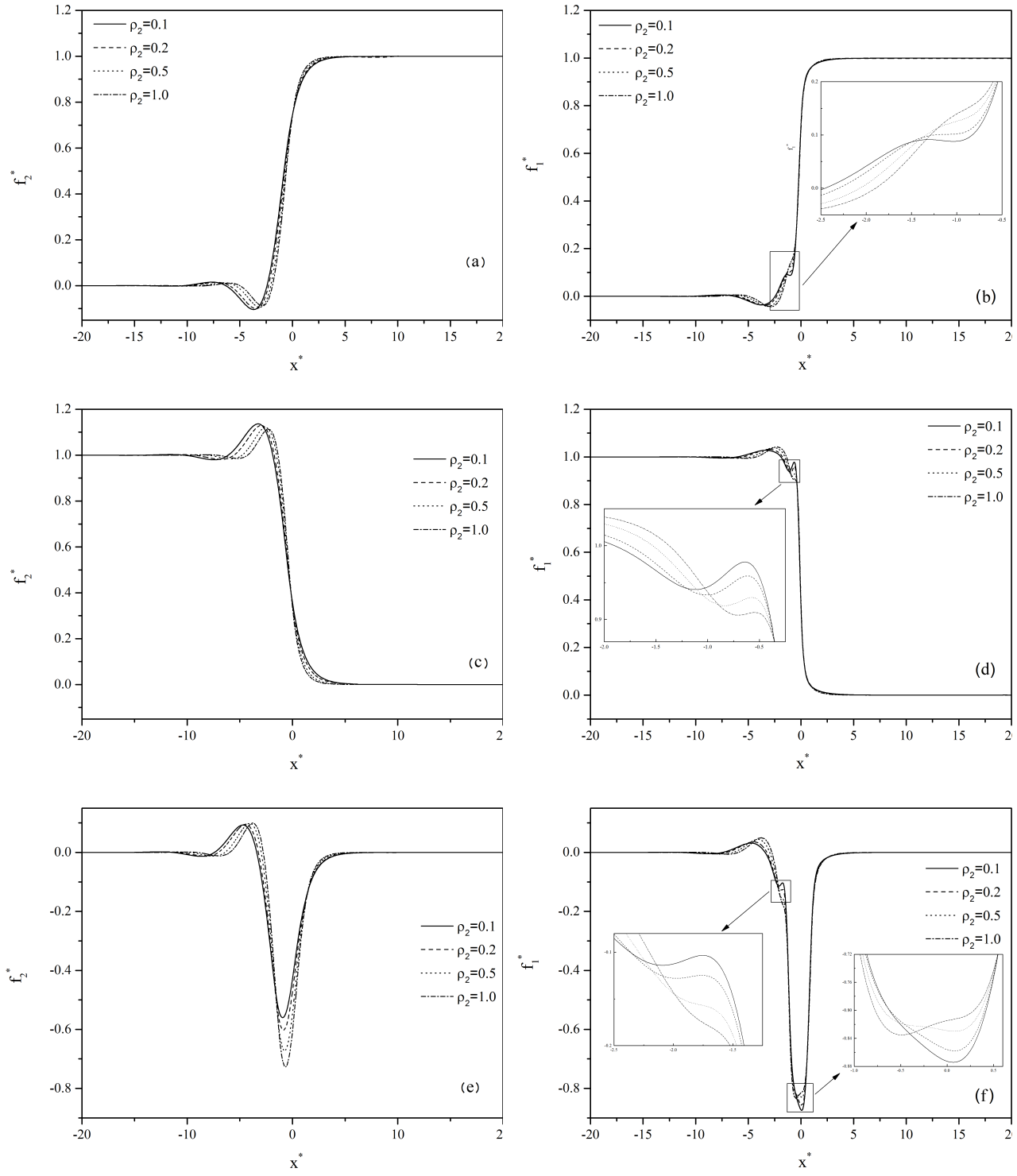

Figure 13: The influence of density ratio on the free surface shape (left column) and liquid-liquid interface (right column) for gravity-driven film flow over a step-up (top row), step-down (middle row) and trench (bottom row) topography when $Re = 0$, $\mu_2 = 1.0$, $|s_0| = 0.2$, $h_{10} = 0.5$, $\theta = 10^\circ$ and $l_t = 1.5$.

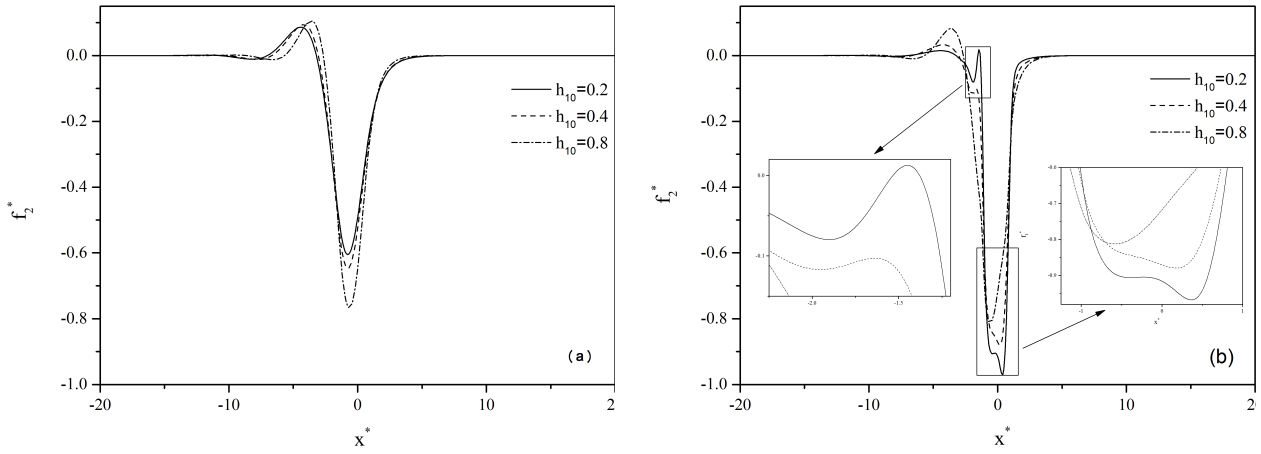

Figure 14: Effect of h_{10} on (a) the free surface shape and (b) the liquid-liquid interface disturbance for gravity-driven film flow over a trench topography, when $Re = 0$, $\rho_2 = 0.5, \mu_2 = 1.0$, $|s_0| = 0.2$ and $\theta = 10°$.

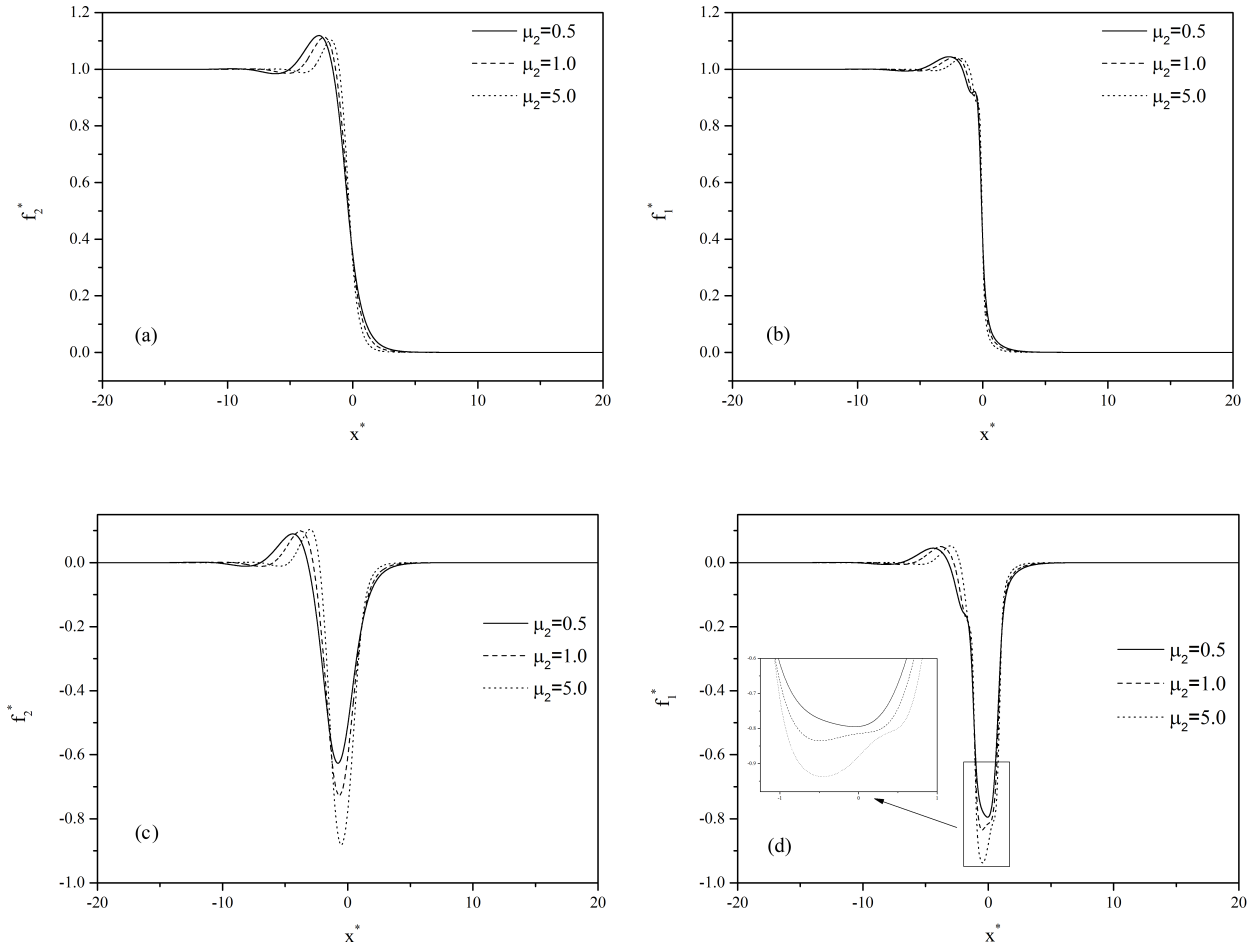

Figure 15: Influence of viscosity on the free surface shape (left column) and liquid-liquid interface disturbance (right column) for gravity-driven film flow over step-down (top row) and trench (bottom row) topographies, when Re $= 0$, $|s_0| = 0.2$ $\rho_2 = 1$, $h_{10} = 0.5$ and $\theta = 10°$.

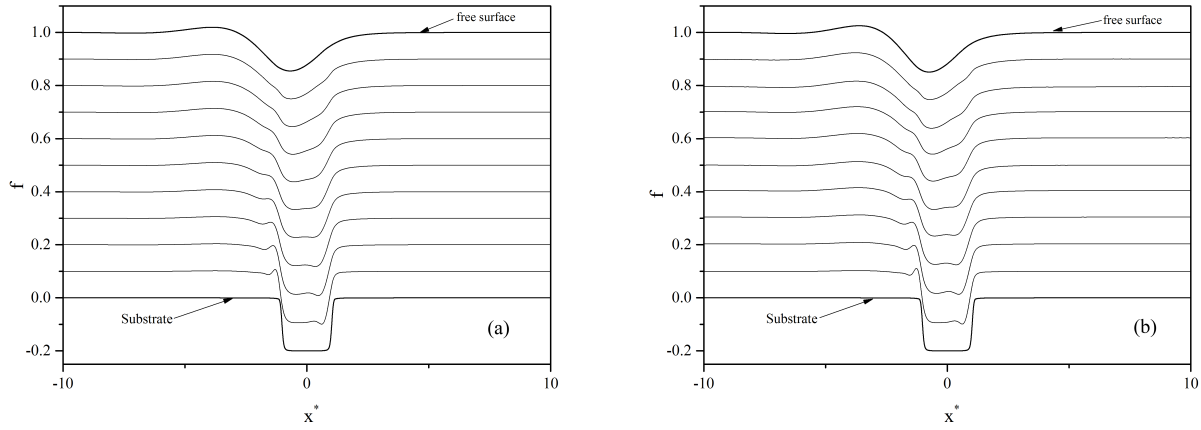

Figure 16: Evolution of the liquid-liquid interface profile for different interface heights as a proportion of the overall bilayer thickness, for gravity-driven film flow over a trench topography when $|s_0| = 0.2$, $\rho_2 = \mu_2 = 1$ and $\theta = 10°$: (a)$Re = 0$; (b)$Re = 15$.

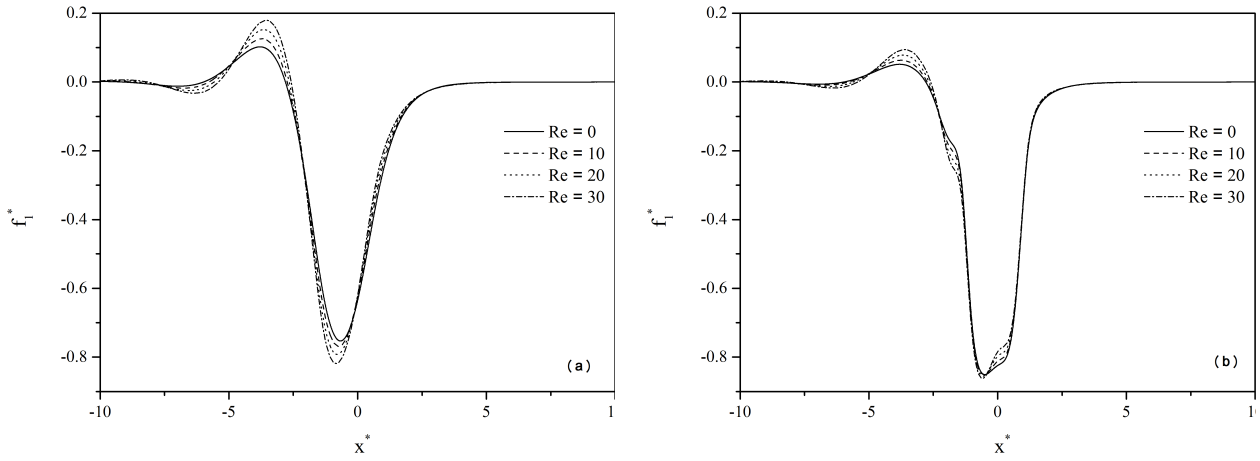

Figure 17: Effect of Re on the (a) the free surface shape and (b) the liquid-liquid interface for gravity-driven film flow over trench topography, when $\rho_2 = \mu_2 = 1.0$, $h_{10} = 0.5$, $|s_0| = 0.2$, $l_t = 1.5$ and $\theta = 10°$.

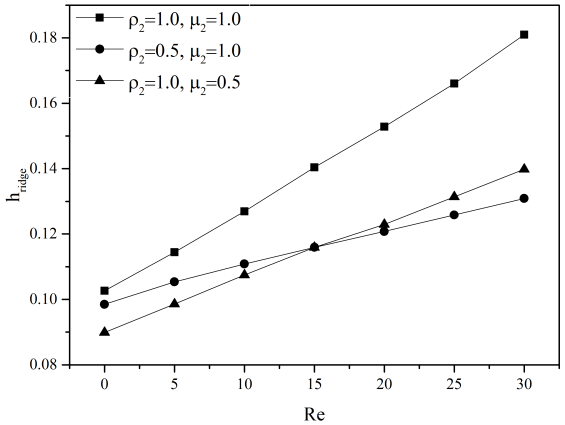

Figure 18: Change in free-surface capillary ridge height as a function of Re for gravity-driven film flow over trench topography for different combinations of ρ_2 and μ_2, when $h_{10} = 0.5$, $|s_0| = 0.2$, $l_t = 1.5$ and $\theta = 10°$.

References

[1] Tabeling, P., Introduction to Microfluidics., Oxford University Press, Oxford, 2005.

[2] Kang, B., Lee, W.H., Cho, K., Recent advances in organic transistor printing processes., ACS Appl. Mater. Interfaces 5 (7) (2013) 2302–2315.

[3] Müller, C.D., Falcou, A., Reckefuss, N., Rojahn, M., Wiederhirn, V., Rudati, P., Frohne, H., Nuyken, O., Becker, H., Meerholz, K., Multi-colour organic light-emitting displays by solution processing., Nature 421 (6925) (2003) 829–833.

[4] Mandal, S., Dell'erba, G., Luzio, A., Bucella, S.G., Perinot, A., Calloni, A., Berti, G., Bussetti, G., Duò, L., Facchetti, A., Noh, Y.-Y., Caironi, M., Fully-printed, all-polymer, bendable and highly transparent complementary logic circuits., Org. Electron. 20 (2015) 132–141.

[5] Kistler, S.F., Schweizer, P.M (Eds.), Liquid Film Coating., Chapman and Hall, 1997.

[6] Vlachogiannis, M., Bontozoglou, V., Experiments on laminar film flow along a periodic wall., J. Fluid Mech. 457 (2002) 133–156.

[7] Decré, M.M.J., Baret, J.C., Gravity-driven flows of viscous liquids over two-dimensional topographies., J. Fluid Mech. 487 (2003) 147–166.

[8] Wierschem, A., Scholle, M., Aksel, N., Vortices in film flow over strongly undulated bottom profiles at low Reynolds numbers., Phys. Fluids 15 (2) (2003) 426–435.

[9] Wierschem, A., Aksel, N., Influence of inertia on eddies created in films creeping over strongly undulated substrates., Phys. Fluids 16 (12) (2004) 4566–4574.

[10] Stillwagon, L.E., Larson, R.G., Fundamentals of topographic substrate leveling., J. Appl. Phys. 63 (11) (1988) 5251–5258.

[11] Peurrung, L.M., Graves, D.B., Film thickness profiles over topography in spin coating., J. Electrochem. Soc. 138 (7) (1991) 2115–2124.

[12] Kalliadasis, S., Bielarz, C., Homsy, G.M., Steady free-surface thin film flows over topography., Phys. Fluids 12 (8) (2000) 1889–1898.

[13] Hayes, M., O'Brien, S.B.G., Lammers, J.H., Green's function for steady flow over a small two-dimensional topography., Phys. Fluids 12 (11) (2000) 2845–2858.

[14] Gaskell, P.H., Jimack, P.K., Sellier, M., Thompson, H.M., Wilson, M.C.T., Gravity-driven flow of continuous thin liquid films on non-porous substrates with topography., J. Fluid Mech. 509 (2004) 253–280.

[15] Scholle, M., Haas, A., Aksel, N., Wilson, M.C.T., Thompson, H.M., Gaskell, P.H., Competing geometric and inertial effects on local flow structure in thick gravity-driven fluid films., Phys. Fluids 20 (12) (2008) 123101.

[16] Bontozoglou, V., Serifi, K., Falling film flow along steep two-dimensional topography: The effect of inertia., Int. J. Multiphas. Flow 34 (8) (2008) 734–747.

[17] Veremieiev, S., Thompson, H.M., Gaskell, P.H., Free-surface film flow over topography: full three-dimensional finite element solutions., Comput. Fluids 122 (2015) 6682.

[18] Mazouchi, A., Homsy, G.M., Free surface Stokes flow over topography., Phys. Fluids 13 (10) (2001) 2751–2761.

[19] Scholle, M., Wierschem, A., Aksel, N., Creeping films with vortices over strongly undulated bottoms., Acta Mech. 168 (3-4) (2004) 167–193.

[20] Blyth, M.G., Pozrikidis, C., Film flow down an inclined plane over a three-dimensional obstacle., Phys. Fluids 18 (5) (2006) 052104.

[21] Baxter, S.J., Power, H., Cliffe, K.A., Hibberd, S., Three-dimensional thin film flow over and around an obstacle on an inclined plane., Phys. Fluids 21 (3) (2009) 032102.

[22] Lenz, R.D., Kumar, S., Steady two-layer flow in a topographically patterned channel., Phys. Fluids 19 (2007) 102103.

[23] Zhou, C., Kumar, S., Two-dimensional two-layer channel flow near a step., Chem. Eng. Sci. 81 (2012) 38–45.

[24] Lenz, R.D., Kumar, S., Instability of confined thin liquid film trilayers., J. Colloid Interf. Sci. 316 (2) (2007) 660–670.

[25] Khayat, R.E., Tian, G., Steady two-layer flow in narrow channels of variable width., Phys. Rev. E 79 (4) (2009) 046326.

[26] Sellier, M., Lenz, R.D., A note on approximate benchmark solutions for viscous two-layer flows., Anziam Journal 51 (4) (2010) 406–415.

[27] Yih, C.-S., Instability due to viscosity stratification., J. Fluid Mech. 27 (02) (1967) 337–352.

[28] Kao, T.W., Stability of two-layer viscous stratified flow down an inclined plane., Phys. Fluids 8 (5) (1965) 812–820.

[29] Kao, T.W., Role of viscosity stratification in the stability of two-layer flow down an incline., J. Fluid Mech. 33 (03) (1968) 561–572.

[30] Yih, C.-S., Stability of liquid flow down an inclined plane., Phys. Fluids 6 (3) (1963) 321–334.

[31] Loewenherz, D.S., Lawrence, C.J., The effect of viscosity stratification on the stability of a free surface flow at low reynolds number., Phys. Fluids A 1 (10) (1989) 1686–1693.

[32] Chen, K.P., Wave formation in the gravity-driven low-Reynolds number flow of two liquid films down an inclined plane., Phys. Fluids A 5 (12) (1993) 3038–3048.

[33] Hu, J., Millet, S., Botton, V., Hadid, H.B., Henry, D., Inertialess temporal and spatio-temporal stability analysis of the two-layer film flow with density stratification., Phys. Fluids 18 (10) (2006) 104101.

[34] Hu, J., Yin, X.Y., Hadid, H.B., Henry, D., Linear temporal and spatiotemporal stability analysis of two-layer falling films with density stratification., Phys. Rev. E 77 (2) (2008) 026302.

[35] Gaurav, Shankar, V., Role of wall deformability on interfacial instabilities in gravity-driven two-layer flow with a free surface., Phys. Fluids 22 (9) (2010) 094103.

[36] Alba, K., Khayat, R.E., Pandher, R.S., Steady two-layer gravity-driven thin-film flow., Phys. Rev. E 77 (5) (2008) 056304.

[37] Shkadov, V.Y., Wave flow regimes of a thin layer of viscous fluid subject to gravity., Izv. Akad. Nauk SSSR Fluid Dynamics 2 (1) (1967) 29–34.

[38] Oron, A., Davis, S.H., Bankoff, S.G., Long-scale evolution of thin liquid films., Rev. Mod. Phys. 69 (3) (1997) 931–980.

[39] Van Oss, C.J., Chaudhury, M.K., Good, R.J., Interfacial lifshitz-van der waals and polar interactions in macroscopic systems., Chem Rev. 88 (6) (1988) 927–941.

[40] Israelachvili, J.N., Intermolecular and surface forces: revised third edition., Academic press, 2011.

[41] Shkadov, V.Y., Wave-flow theory for a thin viscous liquid layer., Izv. Akad. Nauk SSSR Fluid Dynamics 3 (2) (1968) 12–15.

[42] Ruyer-Quil, C., Manneville, P., Modeling film flows down inclined planes., Eur. Phys. J. B. 6 (2) (1998) 277–292.

[43] Ruyer-Quil, C., Manneville, P., Improved modeling of flows down inclined planes., Eur. Phys. J. B. 15 (2) (2000) 357–369.

[44] Ruyer-Quil, C., Manneville, P., Further accuracy and convergence results on the modeling of flows down inclined planes by weighted-residual approximations., Phys. Fluids 14 (1) (2002) 170–183.

[45] Nguyen, L.T., Balakotaiah, V., Modeling and experimental studies of wave evolution on free falling viscous films., Phys. Fluids 12 (9) (2000) 2236–2256.

[46] Amaouche, M., Mehidi, N., Amatousse, N., An accurate modeling of thin film flows down an incline for inertia dominated regimes., Eur. Phys. J. B. 24 (1) (2005) 49–70.

[47] Veremieiev, S., Thompson, H.M., Lee, Y.C., Gaskell, P.H., Inertial thin film flow on planar surfaces featuring topography., Comput. Fluids 39 (3) (2010) 431–450.

[48] Veremieiev, S., Gravity-driven continuous thin film flow over topography., Ph.D. thesis, University of Leeds (2011).

[49] Chapra, S.C., Canale, R.P., Numerical Methods for Engineers., 4th Edition, McGraw-Hill, New York, 2002.

[50] Stillwagon, L.E., Larson, R.G., Leveling of thin-films over uneven substrates during spin coating., Phys. Fluids A 2 (11) (1990) 1937–1944.

[51] Harlow, F.H., Welch, J.E., et al., Numerical calculation of time-dependent viscous incompressible flow of fluid with free surface., Phys. Fluids 8 (12) (1965) 2182–2189.

[52] Abdalla, A.A., Bilayer channel and free surface thin film flow over topography., Ph.D. thesis, University of Leeds (2014).

[53] Trottenberg, U., Oosterlee, C.W., Schüller, A., Multigrid., Academic Press, 2001.

[54] Patankar, S., Numerical heat transfer and fluid flow., CRC Press, 1980.

[55] Chung, T.J., Computational Fluid Dynamics., Cambridge University Press, Cambridge, 2002.

[56] Lee, Y.C., Thompson, H.M., Gaskell, P.H., An efficient adaptive multigrid algorithm for predicting thin film flow on surfaces containing localised topographic features., Comput. Fluids 36 (5) (2007) 838–855.

[57] Gaskell, P.H., Lee, Y.C., Thompson, H.M., Thin film flow over and around surface topography: a general solver for the long-wave approximation and related equations., CMES-Comp. Model. Eng. Sci. 62 (1) (2010) 77–112.

[58] Slade, D., Gravity-driven thin liquid films: rivulets and flow dynamics., Ph.D. thesis, University of Leeds (2013).

[59] Amaouche, M., Mehidi, N., Amatousse, N., Linear stability of a two-layer film flow down an inclined channel: A second-order weighted residual approach., Phys. Fluids 19 (8) (2007) 084106.

[60] Bertozzi, A.L., Brenner, M.P., Linear stability and transient growth in driven contact lines., Phys. Fluids 9 (3) (1997) 530–539.

[61] Saprykin, S., Koopmans, R.J., Kalliadasis, S., Free-surface thin-film flows over topography: influence of inertia and viscoelasticity., J. Fluid Mech. 578 (2007) 271–293.

[62] Scott, J.A., Ma42 element-a state-of-the-art frontal solver for finite-element applications., Tech. rep., Council for the Central Laboratory of the Research Councils (2004).

[63] Benjamin, T.B., Wave formation in laminar flow down an inclined plane., J. Fluid Mech. 2 (6) (1957) 554–574.

[64] Wierschem, A., Lepski, C., Aksel, N., Effect of long undulated bottoms on thin gravity-driven films., Acta Mech. 179 (1-2) (2005) 41–66.

[65] Argyriadi, K., Vlachogiannis, M., Bontozoglou, V., Experimental study of inclined film flow along periodic corrugations: The effect of wall steepness., Phys. Fluids 18 (1) (2006) 012102.

[66] Cao, Z., Vlachogiannis, M., Bontozoglou, V., Experimental evidence for a short-wave global mode in film flow along periodic corrugations., J. Fluid Mech. 718 (2013) 304–320.

[67] Pollak, T., Aksel, N., Crucial flow stabilization and multiple instability branches of gravity-driven films over topography., Phys. Fluids 25 (2) (2013) 024103.

[68] Schörner, M., Reck, D., Aksel, N., Stability phenomena far beyond the nusselt flowrevealed by experimental asymptotics., Phys. Fluids 28 (2) (2016) 022102.

[69] Schörner, M., Reck, D., Aksel, N., Trifonov, Y., Switching between different types of stability isles in films over topographies., Acta Mech. (2017) 1–14.

[70] Schweizer, P.M., Visualization of coating flows., Journal of fluid mechanics 193 (1988) 285–302.

[71] Apps, C.J., Slot exit flow phenomena in industrial slide-fed coating systems, Ph.D. thesis, University of Leeds (2000).

[72] Noakes, C.J., Gaskell, P.H., Thompson, H.M., Ikin, J.B., Streak-line defect minimization in multi-layer slide coating systems., Chem. Eng. Res. Des. 80 (5) (2002) 449–463.

[73] Bermel, M.S., McKeown, S.P., Ruschak, K.J., Slide bead coating with a low viscosity carrier layer, US Patent 6,579,569 (Jun. 17 2003).

[74] Ikin, J.B., An experimental analysis of carrier layer flows, Ph.D. thesis, University of Leeds (2005).

[75] Spurk, J.H., Aksel, N., Fluid Mechanics., 2nd Edition, Academic Press, Springer, 2008.